Lattice models in micromechanics

Martin Ostoja-Starzewski

Department of Mechanical Engineering, McGill University, 817 Sherbrooke St West, Montréal, Québec, Canada H3A 2K6; martin.ostoja@mcgill.ca

This review presents the potential that lattice (or spring network) models hold for micromechanics applications. The models have their origin in the atomistic representations of matter on one hand, and in the truss-type systems in engineering on the other. The paper evolves by first giving a rather detailed presentation of one-dimensional and planar lattice models for classical continua. This is followed by a section on applications in mechanics of composites and key computational aspects. We then return to planar lattice models made of beams, which are a discrete counterpart of non-classical continua. The final two sections of the paper are devoted to issues of connectivity and rigidity of networks, and lattices of disordered (rather than periodic) topology. Spring network models offer an attractive alternative to finite element analyses of planar systems ranging from metals, composites, ceramics and polymers to functionally graded and granular materials, whereby a fiber network model of paper is treated in considerable detail. This review article contains 81 references. [DOI: 10.1115/1.1432990]

INTRODUCTION

Lattice (or spring network) models are based, in principle, on the atomic lattice models of materials. These models work best when the material may naturally be represented by a system of discrete units interacting via springs, or, more generally, rheological elements. It is not surprising that spatial trusses and frameworks have been the primary material systems thus modeled. In the case of granular media, the lattice methods are called discrete element models. Spring networks can also be used to model continuum systems by a lattice much coarser than the true atomic one—the idea dates back, at least, to Hrennikoff [1], if not to Maxwell [2] in a special setting of optimal trusses. This coarse lattice idea obviates the need to work with the enormously large number of degrees of freedom that would be required in a true lattice model, and allows a very modest number of nodes per single heterogeneity (eg, inclusion in a composite, or grain in a polycrystal). As a result, spring networks are a close relative of the much more widespread finite element method.

In this paper, we focus on basic concepts and applications of spring networks, in particular, to anti-plane elasticity, planar classical elasticity, and planar micropolar elasticity. Two settings of such models are elaborated in some detail: periodic lattices and those with disordered topologies. We also indicate connections with other, related studies such as generic rigidity in the field of structural topology. Additionally, an adaptation of lattice methods to modeling crack propagation are presented. This spring network models are sufficiently general to apply to systems ranging from metals, composites, ceramics and polymers to functionally graded and granular materials. The most extensive example treated here is that of mechanics of paper from the standpoint of a disordered network of cellulose, beam-type fibers.

1 ONE-DIMENSIONAL LATTICES

1.1 Simple lattice and elastic string

Let us first consider a lattice-based derivation of a wave equation for a one-dimensional (1D) chain of particles; see also [3]. The particles (parametrized by i), each of mass m_i, interact via nearest-neighbor springs, Fig. 1. For the potential and kinetic energies we find

$$U=\frac{1}{2}\sum_i F_i(u_{i+1}-u_i)=\frac{1}{2}\sum_i K(u_{i+1}-u_i)^2$$

$$T=\frac{1}{2}\sum_i m\dot{u}_i^2 \tag{1.1}$$

where $F_i=K(u_{i+1}-u_i)$ is the axial force at i, and K is the spring constant between i and $i+1$. Using the Euler-Lagrange equations for the Lagrangian $L=T-U$, we arrive at the dynamical equations

$$K(u_{i+1}-2u_i+u_{i-1})=m\ddot{u}_i \tag{1.2}$$

which describe a system of coupled oscillators. By taking a Taylor expansion up to the second derivative for the displacement $u_{i\pm1}\equiv u(x_i\pm s)$,

$$u_{i\pm1}\cong u|_{x_i}\pm u_{,x}|_{x_i}s+\frac{1}{2!}u_{,xx}\Big|_{x_i}s^2 \tag{1.3}$$

Transmitted by Associate Editor RB Hetnarski

we find from Eq. (1.2) an approximating continuum mechanics model, *ie*, a basic wave equation

$$EAu_{,xx}=\rho A\ddot{u} \tag{1.4}$$

where (A being the cross-sectional area of the rod)

$$E=\frac{Ks}{A} \quad \rho=\frac{m}{As}. \tag{1.5}$$

Of course, Eq. (1.4) can also be obtained from the Hamilton's principle for the Lagrangian L expressed in terms of continuum-like quantities, by first introducing Eq. (1.3) in $(1.1)_1$ with terms up to the first derivative,

$$U=\frac{AE}{2}\int_0^d (u_{,x})^2 dx \quad T=\frac{A\rho}{2}\int_0^d (\dot{u})^2 dx. \tag{1.6}$$

1.2 Micropolar lattice and elastic beam

We now generalize the preceding lattice model to describe transverse motions of a 1D chain of dumbbell particles (rigid bars) pin-connected by central-force (axial) springs, Fig. 2. We need to consider two degrees of freedom per particle i: total transverse displacement w_i and rotation φ_i. The constitutive laws for a single bay (between i and $i+1$) are

$$\tilde{F}_i=K_\perp(w_{i+1}-w_i-s\varphi_{i+1}) \quad M_i=-\hat{K}(\varphi_{i+1}-\varphi_i). \tag{1.7}$$

Here $\tilde{F}_i$ is shear force and M_i is bending moment at i, whereby the term $\varphi_{i+1}s$ is subtracted in Eq. $(1.7)_1$ to so as to deal with shear only. For this 1D chain of particles, we write down potential and kinetic energies

$$U=\frac{1}{2}\sum_i K_\perp[w_{i+1}-w_i-s\varphi_{i+1}]^2+\hat{K}(\varphi_{i+1}-\varphi_i)^2$$

$$T=\frac{1}{2}\sum_i m\dot{w}_i^2+J\dot{\varphi}_i^2. \tag{1.8}$$

The first term in Eq. $(1.8)_1$ accounts for shear deformations, while the second for bending.

Using the Euler-Lagrange equations for the Lagrangian $L=T-U$, we obtain a system of equations

$$K_\perp[w_{i+1}-2w_i+w_{i-1}-s(\varphi_{i+1}-\varphi_i)]=m\ddot{w}_i$$

$$\hat{K}[\varphi_{i+1}-2\varphi_i+\varphi_{i-1}]+K_\perp[w_{i+1}-w_{i-1}-s\varphi_i]s=J\ddot{\varphi}_i. \tag{1.9}$$

By introducing the Taylor expansions for w_i and φ_i in Eq. $(1.9)_1$ with terms up to the second derivative, and taking the limit $s\to 0$, we find

$$GA[w_{,x}-\varphi]_{,x}=\rho A\ddot{w}$$

$$EI\varphi_{,xx}+GA[w_{,x}-\varphi]=\rho I\ddot{\varphi} \tag{1.10}$$

where (A and I being the area and second moment of cross-section of the beam-like lattice)

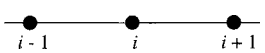

Fig. 1 A 1D chain of particles of lattice spacing s, connected by axial springs (thin lines)

$$G=\frac{K_\perp s}{A} \quad \rho=\frac{m}{As} \quad I=\frac{JA}{m} \quad E=\frac{\hat{K}sm}{JA}. \tag{1.11}$$

Equations (1.10) are recognized as the equations of a Timoshenko beam. Evidently, this is a 1D micropolar continuum with two degrees of freedom: displacement w and rotation φ.

As in Section 1.1, Eq. (1.10) could alternatively be obtained by first introducing Taylor series with terms up to the first derivative into Eq. (1.8) to first get

$$U=\frac{1}{2}\int_0^d [GA(w_{,x})^2+EI(\varphi_{,x})^2]dx$$

$$T=\frac{1}{2}\int_0^d [A\rho(\dot{w})^2+I\rho(\dot{\varphi})^2]dx \tag{1.12}$$

and then, by employing the Hamilton's principle.

A question arises here: Can other, more complex (micro) structures, especially those made of little beams connected by rigid joints, of a general beam-like geometry-such as shown in Fig. 3 be sufficiently well described by this beam model? The general answer is *no*. (see eg, [4]). The basic procedure, however, recommended by that author is basically the same as that outlined here:

1) the equivalent micropolar beam model is set up from the postulate of the same strain and kinetic energies stored in the original lattice when both are deformed identically;
2) a typical repeating element is identified and the energies for this element are expressed in terms of the nodal displacements, joint rotations, as well as the geometric and material properties of the individual members;
3) a passage to an effective continuum is carried out via a Taylor expansion, whereby it turns out that higher-order terms show up in the governing continuum equations, depending on the actual microgeometry of the rods making up the structure; see also [5].

It is appropriate to note here that beam-like lattices can also be analyzed by a cell transfer matrix approach—the eigenvalues of this matrix are the decay rates relevant in the Saint-Venant's principle for these discrete, rather than continuum, systems [6]. The associated eigenvectors and principal vectors lead to equivalent continuum-beam properties. We end by noting that continuum approximations of plate-like structures were also investigated [7]. In that review, among the problems needing new investigations was also listed the effect of microstructural material randomness.

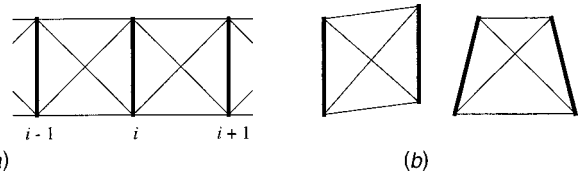

Fig. 2 *a*) A 1D chain of dumbbell particles (vertical rigid bars) of X-braced girder geometry, pin-connected by axial springs (thin lines); and *b*) the shear and curvature modes of a single bay

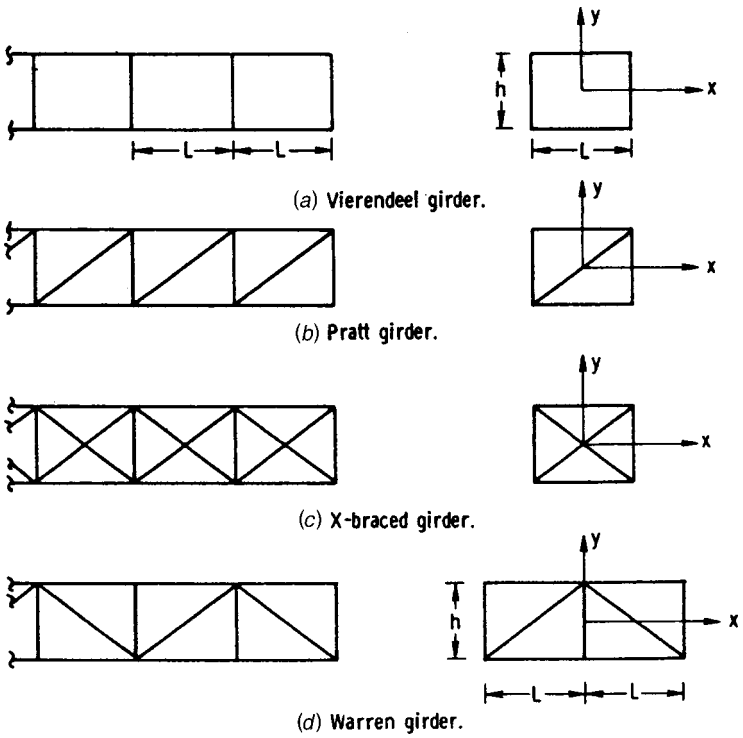

Fig. 3 Planar lattices and their repeating elements (after Noor and Nemeth [4])

1.3 Axial-twisting coupling and dynamics of a helix

Suppose we have a wire rope helically wound along the x_1-axis [8] (Fig. 4). We need then to consider a coupling between the axial force F and torque M on one hand, and the axial strain ε and rotational strain $\beta = R\tau_S$ on the other, that is

$$F = C_{11}\varepsilon + C_{12}\beta \quad M = C_{21}\varepsilon + C_{22}\beta. \tag{1.13}$$

Here, from a requirement of a positive strain energy density, we obtain two conditions on four constitutive coefficients C_{ij}

$$C_{11} > 0 \quad C_{22} > 0 \quad C_{12} = C_{21} \quad C_{11}C_{22} - C_{12}C_{21} > 0. \tag{1.14}$$

In the language of continuum mechanics, the wire rope is a 1D micropolar medium of a *noncentrosymmetric* type. In studies of 2D and 3D models of such continua these terms are also used: *hemitropic*, *antisymmetric*, or *chiral composite* [9,10]. Interestingly, while the Timoshenko beam involved a shear force and a moment normal to the beam's axis, and also mutually orthogonal, in the present model the axial force and moment are parallel to the main axis.

It is important to note that Eqs. (1.13) apply to other physical systems than a wire rope, for example: *i*) a wood fiber made of helically wound fibrils, and *ii*) a simple helix. Indeed, description (1.13) holds, regardless of whether the derivation of the C_{ij} coefficients is made from the standpoint of a theory of a bundle of wires or a continuum shell. Indeed, it was shown, in the context of structural mechanics [11], that either assumption would lead to a few percent difference (at most ~11%) for any of these coefficients. It remains to be seen, however, what those differences would be for a shell made of a large number of thin cellulose fibrils winding along the axis of a cellulose fiber rather than a few thick wires such as shown in Fig. 4.

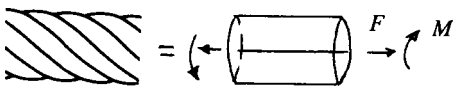

Fig. 4 A wire rope of constant helix angle

The constitutive equations (1.13) in combination with the balance equations led Samras *et al* [12] to derive a system of two coupled wave equations governing the axial-twisting response of a fiber

$$C_{11}u_{,xx} + C_{12}\varphi_{,xx} = \rho\ddot{u} \quad C_{21}u_{,xx} + C_{22}\varphi_{,xx} = J\ddot{\varphi} \tag{1.15}$$

where ρ is the mass density and J is the mass polar moment of inertia. These authors considered a monochromatic wave propagation along the fiber

$$u(x,t) = U\exp[ik(x-ct)] \quad \varphi(x,t) = \Phi\exp[ik(x-ct)] \tag{1.16}$$

and arrived at a dispersion relation resulting in two wave speeds

$$c_{1,2} = \frac{2(C_{11}C_{22} - C_{12}C_{21})}{(C_{11}J + C_{22}\rho) \pm [(C_{11}J - C_{22}\rho)^2 + 4\rho J C_{12}C_{21}]^{1/2}}. \tag{1.17}$$

It followed, by inspection, that $c_1 < c_2$, and, in fact, there may be an order of magnitude difference between both wave speeds. In view of Eq. (1.16), axial vibrations of the fiber are described by two types of waves—slow and fast—each of which consists of forward and backward going pulses

$$u(x,t)=U_1e^{ik(x-c_1t)}+U_2e^{ik(x+c_1t)}+U_3e^{ik(x-c_2t)}+U_4e^{ik(x+c_2t)}$$

$$\varphi(x,t)=\Phi_1e^{ik(x-c_1t)}+\Phi_2e^{ik(x+c_1t)}+\Phi_3e^{ik(x-c_2t)}+\Phi_4e^{ik(x+c_2t)}. \quad (1.18)$$

Next, by considering the ratio of axial to torsional amplitudes U/Φ, they concluded that the waves that are primarily axial in nature ($U/\Phi>1$) propagate at speeds c_2, while the waves that are primarily torsional in nature ($U/\Phi<1$) propagate at speeds c_1. Clearly, by assuming $C_{12}=C_{21}=0$ one immediately arrives at two uncoupled wave equations for purely axial and torsional waves, respectively.

2 PLANAR SPRING NETWORKS ON PERIODIC LATTICES: CLASSICAL CONTINUA

2.1 Basic idea of a spring network representation

As already demonstrated in the setting of 1D models, the basic idea in setting up the spring network models is based on the equivalence of strain energy stored in a unit cell (Fig. 5), of volume V, of a network

$$U_{cell}=U_{continuum}. \quad (2.1)$$

The unit cell is a periodically repeating part of the network. Two aspects should be noted here:

1) the choice of the unit cell may be non-unique, see Fig 5;
2) the inner structure of the unit cell is not necessarily 'nicely' ordered—it may be of a disordered microgeometry, with an understanding that it repeats itself in space.

In Eq. (2.1) the energies of the cell and its continuum equivalent, respectively, are

$$U_{cell}=\sum_b E_b=\frac{1}{2}\sum_b^{N_b}(\boldsymbol{F}\cdot\boldsymbol{u})^{(b)} \quad U_{continuum}=\frac{1}{2}\int_V \boldsymbol{\sigma}\cdot\boldsymbol{\varepsilon}dV. \quad (2.2)$$

The superscript b in $(2.2)_1$ stands for the b-th spring (bond), and N_b for the total number of bonds. Our discussion is set in the two-dimensional (2D) setting so that, by a volume we actually mean an area of unit thickness. In the sequel we restrict ourselves to linear elastic springs and spatially linear displacement fields $\boldsymbol{u}$ (ie, uniform strain fields ε), so that Eq. (2.2) will become

$$U_{cell}=\frac{1}{2}\sum_b^{N_b}(k\boldsymbol{u}\cdot\boldsymbol{u})^{(b)} \quad U_{continuum}=\frac{1}{2}\boldsymbol{\varepsilon}\cdot\boldsymbol{C}\cdot\boldsymbol{\varepsilon} \quad (2.3)$$

In Eq. (2.3) $\boldsymbol{u}$ is a generalized spring displacement and k its corresponding spring constant. The next step, that will depend on the particular geometry of the unit element and on the particular model of interactions, will involve making a connection between $\boldsymbol{u}$ and $\boldsymbol{\varepsilon}$, and then deriving $\boldsymbol{C}$ from Eq. (2.1). The corresponding procedures and resulting formulas are given below for several elasticity problems set in the square and triangular network geometries.

2.2 Anti-plane elasticity on square lattice

Of all the elasticity problems, the anti-plane one is the simplest on which to illustrate the spring network idea. In the continuum setting, we thus have the constitutive law

$$\sigma_i=C_{ij}\varepsilon_j \quad i,j=1,2 \quad (2.4)$$

where $\boldsymbol{\sigma}=(\sigma_1,\sigma_2)\equiv(\sigma_{31}^0,\sigma_{32}^0)$ and $\boldsymbol{\varepsilon}=(\varepsilon_1,\varepsilon_2)\equiv(\varepsilon_{31}^0,\varepsilon_{32}^0)$. Upon substitution into the momentum balance law

$$\sigma_{i,i}=0, \quad (2.5)$$

we obtain

$$(C_{ij}u_{,j})_{,i}=0. \quad (2.6)$$

Henceforth, we are interested in approximations of locally homogeneous media, so that the governing equation becomes

$$C_{ij}u_{,ij}=0 \quad (2.7)$$

In the special case of an isotropic medium Eq. (2.7) simplifies to a Laplace equation

$$Cu_{,ii}=0. \quad (2.8)$$

We now discretize the material with a square lattice network, Fig. 5*a*, whereby each node has one degree of freedom

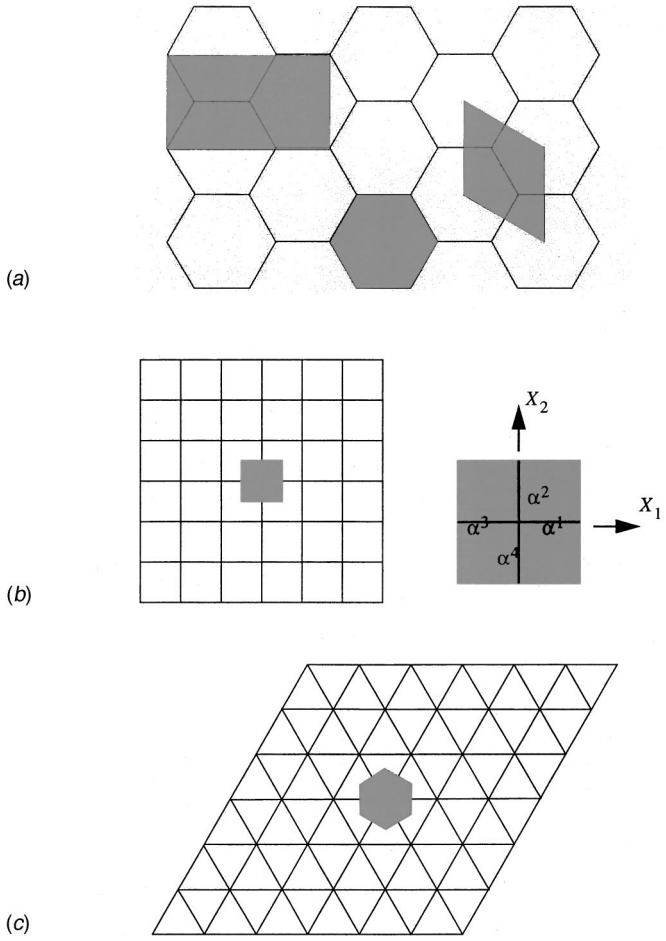

Fig. 5 *a*) A hexagonal lattice with three different choices of unit cell; *b*) a square lattice with a square unit cell; and *c*) a triangular lattice with hexagonal unit cell

(anti-plane displacement u), and nearest neighbor nodes are connected by springs of constant k. It follows that the strain energy of a unit cell of such a lattice is

$$U=\frac{1}{2}k\sum_{b=1}^{4} l_i^{(b)}l_j^{(b)}\varepsilon_i\varepsilon_j . \tag{2.9}$$

In the above, we employed the uniform strain $\varepsilon=(\varepsilon_1,\varepsilon_2)$. Also, $\mathbf{l}^{(b)}=(l_1^{(b)},l_2^{(b)})$ is the vector of half-length of bond b. In view of Eq. (2.1), the stiffness tensor is obtained as

$$C_{ij}=\frac{k}{V}\sum_{b=1}^{4} l_i^{(b)}l_j^{(b)} \quad i,j=1,2 \tag{2.10}$$

where $V=4$ if all the bonds are of unit length ($|\mathbf{l}^{(b)}|=1$). This leads to a relation between the bond spring constant k and the C_{ij} tensor

$$C_{11}=C_{22}=\frac{k}{2} \quad C_{12}=C_{21}=0. \tag{2.11}$$

In order to model an orthotropic medium, different bonds are applied in the x_1 and x_2 directions: $k^{(1)}$ and $k^{(2)}$. The strain energy of a unit cell is now

$$U=\frac{1}{2}\sum_{b=1}^{4} k^{(b)}l_i^{(b)}l_j^{(b)}\overline{\varepsilon_i}\overline{\varepsilon_j} \tag{2.12}$$

so that the stiffness tensor is

$$C_{ij}=\frac{1}{V}\sum_{b=1}^{4} k^{(b)}l_i^{(b)}l_j^{(b)} \tag{2.13}$$

which leads to relations

$$C_{11}=\frac{k^{(1)}}{2} \quad C_{22}=\frac{k^{(2)}}{2} \quad C_{12}=C_{21}=0. \tag{2.14}$$

If one wants to model an anisotropic medium (ie, with $C_{12}\neq 0$), one may either choose to rotate its principal axes to coincide with those of the square lattice and use the network model just described, or introduce diagonal bonds $k^{(5)}$ and $k^{(6)}$ oriented along (1, 1) and (1, −1) directions, respectively. In the latter case, the unit cell energy is given by the formula (2.12) with $N_b=8$. The expressions for C_{ij}'s are

$$C_{11}=\frac{k^{(1)}}{2}+k^{(5)} \quad C_{22}=\frac{k^{(2)}}{2}+k^{(6)} \quad C_{12}=C_{21}=k^{(5)}-k^{(6)}. \tag{2.15}$$

It will become clear in the next section how this model can be modified to a triangular spring network geometry.

2.3 In-plane elasticity: Triangular lattice with central interactions

In the planar continuum setting, which is discussed in some more detail in the Appendix, the isotropic Hooke's law

$$\sigma_{ij}=C_{ijkm}\varepsilon_{km} \quad i,j,k,m=1,2 \tag{2.16}$$

upon substitution into the balance law

$$\sigma_{ij,j}=0 \tag{2.17}$$

results in planar Navier's equation for the displacement u_i

$$\mu u_{i,jj}+\kappa u_{j,ji}=0. \tag{2.18}$$

In Eq. (2.18), μ is defined by $\sigma_{12}=\mu\varepsilon_{12}$, which makes it the same as the classical 3D shear modulus. On the other hand, κ is the (planar) 2D bulk modulus, that is defined by $\sigma_{ii}=\kappa\varepsilon_{ii}$.

As in the foregoing section, we are interested in approximations of locally homogeneous media. Consider a regular triangular network of Fig. 5*b* with central force interactions only, which are described, for each bond b, by

$$F_i=\Phi_{ij}^{(b)}u_j \quad \text{where} \quad \Phi_{ij}^{(b)}=\alpha^{(b)}n_i^{(b)}n_j^{(b)}. \tag{2.19}$$

Similar to the case of anti-plane elasticity, $\alpha^{(b)}$ is the spring constant of half-lengths of such central (normal) interactions, *ie*, of those parts of the springs that lie within the given unit cell. The unit vectors $n^{(b)}$ at respective angles $\theta^{(b)}$ of the first three α springs are

$$\theta^{(1)}=0^\circ \quad n_1^{(1)}=1 \quad n_2^{(1)}=0$$

$$\theta^{(2)}=60^\circ \quad n_1^{(2)}=\frac{1}{2} \quad n_2^{(2)}=\frac{\sqrt{3}}{2}$$

$$\theta^{(3)}=120^\circ \quad n_1^{(3)}=-\frac{1}{2} \quad n_2^{(3)}=\frac{\sqrt{3}}{2}. \tag{2.20}$$

The other three springs ($b=4,5,6$) must, by the requirement of symmetry with respect to the center of the unit cell, have the same properties as $b=1,2,3$, respectively. All the α-springs are of length l, that is, the spacing of the triangular mesh is $s=2l$. The cell area is $V=2\sqrt{3}l^2$.

Every node has two degrees of freedom, and it follows that the strain energy of a unit hexagonal cell of such a lattice, under conditions of uniform strain $\varepsilon=(\varepsilon_{11},\varepsilon_{22},\varepsilon_{12})$, is

$$U=\frac{l^2}{2}\sum_{b=1}^{6} \alpha^{(b)}n_i^{(b)}n_j^{(b)}n_k^{(b)}n_m^{(b)}\varepsilon_{ij}\varepsilon_{km} \tag{2.21}$$

so that, again by Eq. (2.1), the stiffness tensor becomes

$$C_{ijkm}=\frac{l^2}{V}\sum_{b=1}^{6} \alpha^{(b)}n_i^{(b)}n_j^{(b)}n_k^{(b)}n_m^{(b)}. \tag{2.22}$$

In particular, taking all $\alpha^{(b)}$ the same, we see that

$$C_{1111}=C_{2222}=\frac{9}{8\sqrt{3}}\alpha \quad C_{1122}=C_{2211}=\frac{3}{8\sqrt{3}}\alpha$$

$$C_{1212}=\frac{3}{8\sqrt{3}}\alpha \tag{2.23}$$

so that there is only one independent elastic modulus, and the modeled continuum is isotropic.

It is important to note here that the isotropy follows from the triangular lattice having an axis of symmetry of the sixth order. This, combined with the fact that Eq. (2.22) satisfies the conditions of Cauchy symmetry [13] with respect to the permutations of all the four indices

$$C_{ijkm}=C_{ijmk}=C_{jikm}=C_{kmij}=C_{ikjm} \tag{2.24}$$

implies that C_{ijkm} is of the form

$$C_{ijkm}=\lambda(\delta_{ij}\delta_{km}+\delta_{ik}\delta_{jm}+\delta_{im}\delta_{jk}). \tag{2.25}$$

In view of (2.23), we obtain the classical Lamé constants

$$\lambda=\mu=\frac{3}{4\sqrt{3}}\alpha. \tag{2.26}$$

One might try to model anisotropy by considering three different α's in Eq. (2.21), but such an approach would be limited—one needs to have six parameters in order to freely adjust any planar anisotropy which involves six independent C_{ijkm}'s. This can be achieved by introducing the additional angular springs as discussed below. In fact, angular springs are also the device to vary the Poisson's ratio.

2.4 In-plane elasticity: Triangular lattice with central and angular interactions

We continue with the triangular network, and introduce angular springs acting between the contiguous bonds incident onto the same node. These are assigned spring constants $\beta^{(b)}$, and, again by the argument of symmetry with respect to the center of the unit cell, only three of those can be independent. Thus, we arrive at six spring constants: $\{\{\alpha^{(1)},\alpha^{(2)},\alpha^{(3)},\beta^{(1)},\beta^{(2)},\beta^{(3)}\}$. With reference to Fig. 6*b*, let $\Delta\theta^{(b)}$ be the (infinitesimal) angle change of the *b*-th spring orientation from the undeformed position. Noting that, $\mathbf{n}\times\mathbf{n}=\mathbf{l}\Delta\theta$, we obtain

$$\Delta\theta_k^{(b)}=e_{kij}\varepsilon_{jp}n_i n_p \quad i,j,p=1,2 \tag{2.27}$$

where e_{kij} is the Levi-Civita permutation tensor. Since $k=3$, we can simply write $\Delta\theta^{(b)}$ for $\Delta\theta_k^{(b)}$. The angle change between two contiguous α springs (b and $b+1$) is then measured by $\Delta\phi=\Delta\theta^{(b+1)}-\Delta\theta^{(b)}$, so that the energy stored in the spring $\beta^{(b)}$ is

$$\begin{aligned}E^{(b)}&=\tfrac{1}{2}\beta^{(b)}|\Delta\phi|^2\\&=\tfrac{1}{2}\beta^{(2)}\{\varepsilon_{kij}\varepsilon_{jp}(n_i^{(b+1)}n_p^{(b+1)}-n_i^{(b)}n_p^{(b)})\}^2.\end{aligned} \tag{2.28}$$

By superposing the energies of all the angular bonds with the energy (2.21), the elastic moduli are derived as [14]

$$\begin{aligned}C_{ijkm}=&\frac{l^2}{V}\sum_{b=1}^{6}\alpha^{(b)}n_i^{(b)}n_j^{(b)}n_k^{(b)}n_m^{(b)}\\&+\frac{1}{V}\sum_{b=1}^{6}\{(\beta^{(b)}+\beta^{(b-1)})\delta_{ik}n_p^{(b)}n_j^{(b)}n_p^{(b)}n_m^{(b)}\\&-(\beta^{(b)}+\beta^{(b-1)})n_i^{(b)}n_j^{(b)}n_k^{(b)}n_m^{(b)}\\&-\beta^{(b)}\delta_{ik}n_p^{(b)}n_j^{(b+1)}n_p^{(b+1)}n_m^{(b)}\\&+\beta^{(b)}n_i^{(b)}n_j^{(b+1)}n_k^{(b+1)}n_m^{(b)}\\&-\beta^{(b)}\delta_{ik}n_p^{(b)}n_j^{(b)}n_p^{(b+1)}n_m^{(b+1)}\\&+\beta^{(b)}n_i^{(b+1)}n_j^{(b)}n_k^{(b)}n_m^{(b+1)}\}\end{aligned} \tag{2.29}$$

where $b=0$ is the same as $b=6$. This provides the basis for a spring network representation of an anisotropic material; it also forms a generalization of the so-called *Kirkwood model* [15] of an isotropic material. The latter is obtained by assigning the same α to all the normal and the same β to all the angular springs

$$\begin{aligned}C_{ijkm}=&\frac{\alpha}{2\sqrt{3}}\sum_{b=1}^{6}n_i^{(b)}n_j^{(b)}n_k^{(b)}n_m^{(b)}\\&+\frac{\beta}{2\sqrt{3}l^2}\sum_{b=1}^{6}\{2\delta_{ik}n_j^{(b)}n_m^{(b)}-2n_i^{(b)}n_j^{(b)}n_k^{(b)}n_m^{(b)}\\&-\delta_{ik}n_p^{(b)}n_j^{(b+1)}n_p^{(b+1)}n_m^{(b)}+n_i^{(b)}n_j^{(b+1)}n_k^{(b+1)}n_m^{(b)}\\&-\delta_{ik}n_p^{(b)}n_j^{(b)}n_p^{(n+1)}n_m^{(b+1)}\\&+n_i^{(b+1)}n_j^{(b)}n_k^{(b)}n_m^{(b+1)}\}.\end{aligned} \tag{2.30}$$

It follows from the above that

$$\begin{aligned}C_{1111}&=C_{2222}=\frac{1}{2\sqrt{3}}\left(\frac{9}{4}\alpha+\frac{1}{l^2}\beta\right)\\C_{1122}&=C_{2211}=\frac{1}{2\sqrt{3}}\left(\frac{3}{4}\alpha-\frac{1}{l^2}\frac{9}{4}\beta\right)\\C_{1212}&=\frac{1}{2\sqrt{3}}\left(\frac{3}{4}\alpha+\frac{1}{l^2}\frac{9}{4}\beta\right).\end{aligned} \tag{2.31}$$

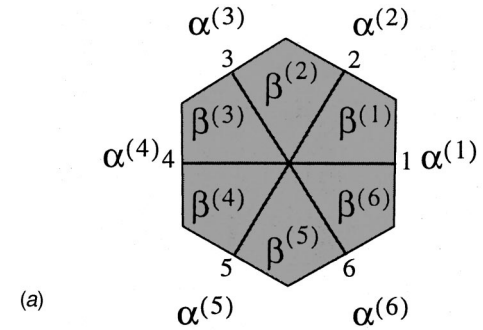

(a)

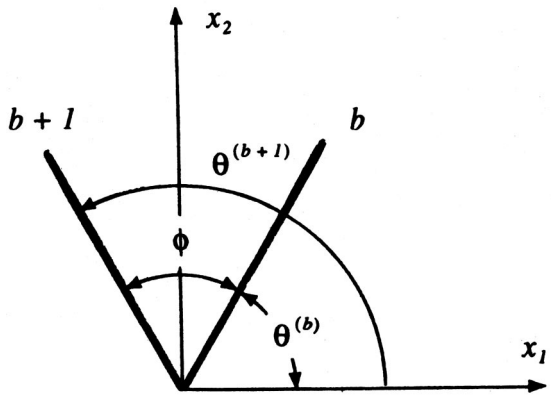

(b)

Fig. 6 *a*) Unit cell of a triangular lattice model; $\alpha^{(1)},\ldots,\alpha^{(6)}$ are the normal spring constants, $\beta^{(1)},\ldots,\beta^{(6)}$ are the angular spring constants; in the isotropic Kirkwood model $\alpha^{(b)}=\alpha^{(b+3)}$ and $\beta^{(b)}=\beta^{(b+3)}$, $b=1,2,3$; and *b*) details of the angular spring model.

Condition $C_{1212}=(C_{1111}-C_{1122})/2$ is satisfied, so that there are only two independent elastic moduli.

From Eq. (2.31), the α and β constants are related to the planar bulk and shear moduli by

$$\kappa=\frac{1}{2\sqrt{3}}\left(\frac{3}{2}\alpha\right) \quad \mu=\frac{1}{2\sqrt{3}}\left(\frac{3}{4}\alpha+\frac{1}{l^2}\frac{9}{4}\beta\right). \tag{2.32}$$

It is noted here that the angular springs have no effect on κ, *ie*, the presence of angular springs does not affect the dilatational response. The formula for a planar Poisson's ratio [16] is

$$\nu=\frac{\kappa-\mu}{\kappa+\mu}=\frac{C_{1111}-2C_{1212}}{C_{1111}}=\left(1-\frac{3\beta}{\alpha l^2}\right)\Big/\left(3+\frac{3\beta}{\alpha l^2}\right). \tag{2.33}$$

From Eq. (2.33), there follows the full range of Poisson's ratio which can be covered with this model. It has two limiting cases

$$\nu=\frac{1}{3} \quad \text{if} \quad \beta/\alpha\to 0 \quad \alpha-\textit{model}$$

$$\nu=-1 \quad \text{if} \quad \beta/\alpha\to\infty \quad \beta-\textit{model}. \tag{2.34}$$

For the subrange of Poisson's ratio between $-1/3$ and $1/3$ one may also use a Keating model [17] which employs a different calculation of the energy stored in angular bonds.

2.5 Triple honeycomb lattice

It is recalled from Section 2.4 that 1/3 is the highest Poisson's ratio of central-force triangular lattices with one spring constant. An interesting model permitting higher values, from 1/3 up to 1, was introduced in [18,19]. The model sets up three honeycomb lattices, having spring constants α, β, and γ, respectively, overlapping in such a way that they form a single triangular lattice, Fig. 7. The planar bulk and shear moduli of a single phase are

$$\kappa=\frac{1}{\sqrt{12}}(\alpha+\beta+\gamma) \quad \mu=\sqrt{\frac{27}{16}}\left(\frac{1}{\alpha}+\frac{1}{\beta}+\frac{1}{\gamma}\right)^{-1}. \tag{2.35}$$

In the case of two or more phases, a spring that crosses a boundary between any two phases 1 and 2 is assigned a spring constant according to a series rule $\alpha=[(2\alpha_1)^{-1}+(2\alpha_2)^{-1}]$, where α_i is a spring constant of the respective phase.

3 APPLICATIONS IN MECHANICS OF COMPOSITES

3.1 Representation by a fine mesh

In order to solve the field equations of a two-phase composite we employ a spring network method, Fig. 8*a*. The idea is to approximate the planar, piecewise-constant continuum by a very fine mesh. In the following, we shall assume that a square mesh in the x_1,x_2-plane for discretization of antiplane displacement field $u\equiv u_3$ is used. The governing equations are

$$u(i,j)[k_r-k_l+k_u+k_d]-u(i+1,j)k_r-u(i-1,j)k_l -u(i,j+1)k_u-u(i,j-1)k_d=f(i,j) \tag{3.1}$$

where $f(i,j)$ is the body force (or source) at the point (i,j), while i and j are the coordinates of mesh points, and k_r, k_l, k_u and k_d are defined from the series spring model

$$k_r=[1/C(i,j)+1/C(i+1,j)]^{-1}$$

$$k_l=[1/C(i,j)+1/C(i-1,j)]^{-1}$$

$$k_u=[1/C(i,j)+1/C(i,j+1)]^{-1}$$

$$k_d=[1/C(i,j)+1/C(i,j-1)]^{-1}. \tag{3.2}$$

In Eq. (3.2), $C(i,j)$ is the property at (i,j).

This type of a discretization is equivalent to a finite difference method that would be derived by considering the expansions

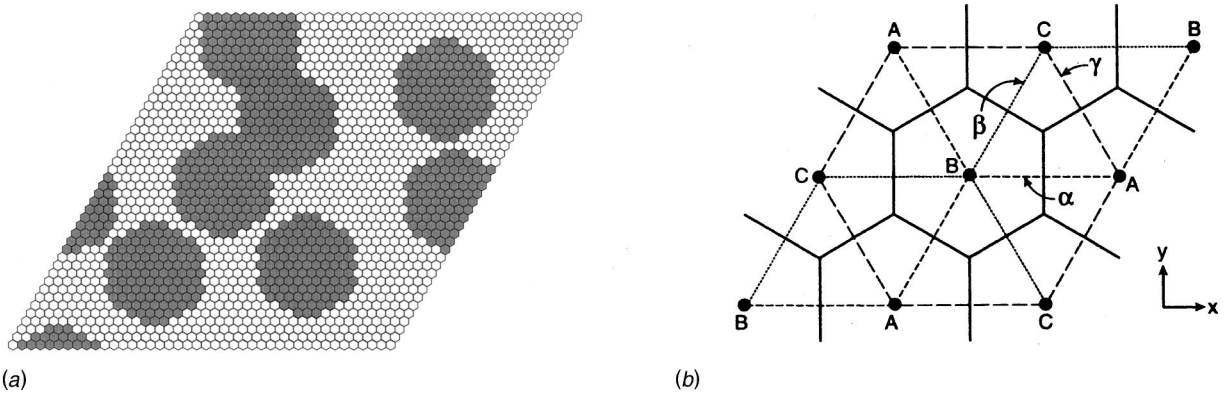

(*a*) (*b*)

Fig. 7 *a*) A triple honeycomb lattice made of three different spring types α, β, and γ belonging, respectively to three sublattices A, B, and C; and *b*) A 42×42 unit cell of a triangular lattice of hexagonal pixels, with 11 pixel diameter circular inclusions centered on pixels and randomly placed with periodic boundary conditions; after Snyder *et al* [19]

$$u(i\pm1,j)=u(i,j)\pm s\frac{\partial}{\partial x_1}(u(i,j))\big|_{i,j}+\frac{s^2}{2!}\frac{\partial^2}{\partial x_1^2}u(i,j)\Big|_{i,j}$$

$$u(i,j\pm1)=u(i,j)\pm s\frac{\partial}{\partial x_2}(u(i,j))\big|_{i,j}+\frac{s^2}{2!}\frac{\partial^2}{\partial x_2^2}u(i,j)\Big|_{i,j} \tag{3.3}$$

in the governing equation (recall (2.8))

$$C\left(\frac{\partial^2 u}{\partial x_1^2}+\frac{\partial^2 u}{\partial x_2^2}\right)=0. \tag{3.4}$$

However, in the case of in-plane elasticity problems, a spring network approach is not identical to a finite difference method, as the node-node connections of a spring network do really have a meaning of springs, whereas the finite difference connections do not.

In the case of a composite made of two locally isotropic phases: matrix (m) and inclusions (i), the Hooke's law is

$$\sigma_i=C_{ij}\varepsilon_j \quad i,j=1,2 \quad C_{ij}=C^{(m)}\delta_{ij} \quad \text{or} \quad C^{(i)}\delta_{ij}. \tag{3.5}$$

The above leads to a so-called *contrast* $C^{(i)}/C^{(m)}$, sometimes also called a *mismatch*. It is clear that by increasing the contrast we can approximately model materials with rigid inclusions. Similarly, by decreasing the contrast, we go to very soft inclusions and nearly reach a system with holes.

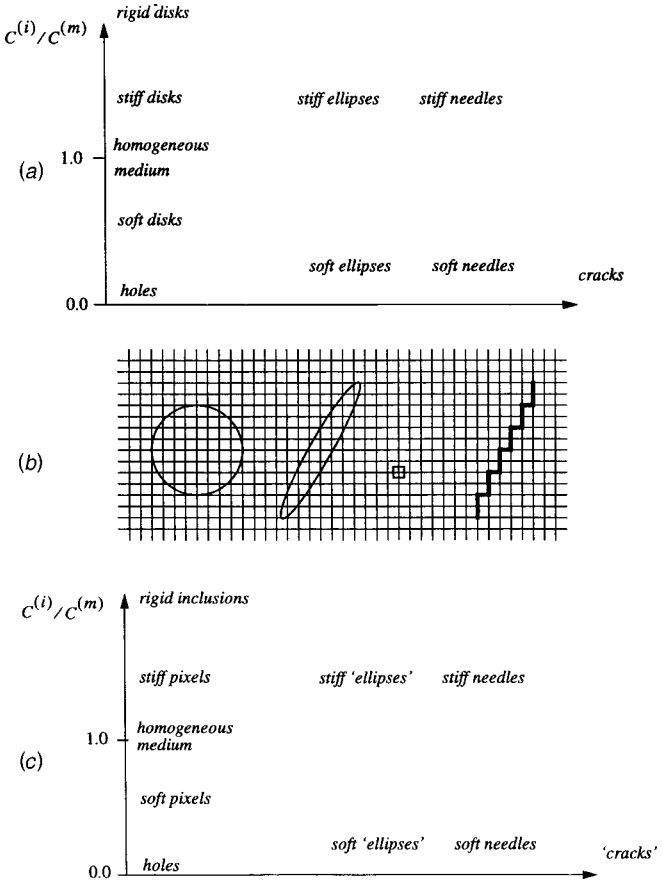

Fig. 8 *a*) Parameter plane: aspect ratio of inclusions and the contrast; *b*) spring network as a basis for resolution of round disks, ellipses, pixels, and needles in the parameter plane; and *c*) another interpretation of the parameter plane: from pixels to needles

While the disk is the most basic inclusion shape when dealing with composites, a departure from this is of interest. Thus, another basic parameter specifying the composite is the *aspect ratio* of ellipses a/b, where $a\,(b)$ is the major (minor) semi-axis. By varying the aspect ratio from 1 up through higher values, we can model systems having disk-type, ellipse-type, through needle-type inclusions. We are thus led to the concept of a parameter plane as shown in Fig. 8*a*.

Resolution of several different types of inclusions by a spring network is shown in Fig. 8*b*. That is, we can model disks, ellipses, needles, etc. Admittedly, this type of modeling is approximate so that a somewhat different interpretation of a parameter plane is given in Fig. 8*c*. It is seen that disks may most simply be modeled as single pixels or more accurately as finite regions; in the latter case arbitrary anisotropies can be modeled. The former case allows one to deal with very large scale systems, while the latter allows a much better resolution of local stress/strain fields within and around the inclusions. By decreasing the spring network mesh size, an increasingly better accuracy can be achieved. Somewhat more accurate results may be obtained by a finite element model, albeit at a higher price of costly and cumbersome remeshing for each and every new disk configuration $B(\omega)$ which is required in statistical studies.

It is noteworthy that, in contradistinction to a finite element method, no need for remeshing and constructing of a stiffness matrix exists in our spring network method: spring constants are very easily assigned throughout the mesh, and the conjugate gradient method finds the solution of the equilibrium displacement field $u(i,j)$. In that manner, a system having 10^6 million degrees of freedom (1000×1000 nodes) can readily be handled on a computer workstation with $\sim$90MB of random access memory. For 2000×2000 nodes, one requires some 360MB, and so on, because of a linear scaling of memory requirements with the number of degrees of freedom.

The quality of approximation of ellipses and needle-type cracks/inclusions can be varied according to the number of nodes chosen to represent such objects. Local fields cannot be perfectly resolved—boundary elements may be better suited for this—but the solution by the spring network is sufficient to rapidly establish the elastic moduli of a number of different $B(\omega)$ realizations from the random medium B, and the corresponding statistics with a sufficient accuracy.

3.2 Solutions of linear algebraic problems

The steady-state conductivity and elastostatics problems on spring networks always lead to linear algebraic systems

$$\boldsymbol{A}\cdot\boldsymbol{x}=\boldsymbol{b} \tag{3.6}$$

because they simply are elliptic problems in discretized forms. There are, in principle, two methods to set up and solve the governing equations. One of them is exactly the same as that conventionally used in the finite element methods—involving the global stiffness matrix accompanied

by the connectivity of all the nodes—and will therefore not be elaborated here. The second one comes, just like the spring networks themselves, from the condensed matter physics. It is the so-called *conjugate gradient* method, which involves the energy of the system as a functional

$$F(\boldsymbol{x}) = \tfrac{1}{2}\, x \cdot \boldsymbol{A} \cdot \boldsymbol{x} - \boldsymbol{b} \cdot \boldsymbol{x} \tag{3.7}$$

of all the relevant degrees of freedom $\boldsymbol{x}$, and the gradient of this energy

$$\nabla F(\boldsymbol{x}) = \boldsymbol{A} \cdot \boldsymbol{x} - \boldsymbol{b} \tag{3.8}$$

with respect to all these degrees. Once written in an explicit form as two subroutines, the program is connected with any of the widely available solvers (see, *eg*, [20]). Note that $F(\boldsymbol{x})$ is minimized when Eq. (3.8) equals zero, which is then equivalent to Eq. (3.6). Of course, one may also employ other algebraic solvers.

It is noteworthy that the entire task of mesh generation, such as typically required by the finite element methods, is absent. The energy and energy gradient subroutines are written once and for all for the given mesh of, say, Fig. 9. The assignment of all the local spring stiffnesses—according to any chosen lattice model of Section 2—is done very rapidly in the first stage of the program. These stiffnesses are stored in the common block (in case of a Fortran program) and are readily accessible to the conjugate gradient subroutines that are activated in the second, and main, stage of the program. Once the energy minimum is reached to within any specified accuracy, this energy is used to compute the overall, effective moduli of a given domain of the lattice based on the postulate of the energy equivalence, see *eg*, [21–23].

Here we list several exact relations that may be used in testing the resulting computer programs. Some of them, as well as others, are also elaborated in [24].

i) Suppose we have solutions of two elasticity problems on a certain domain B, with boundary ∂B, corresponding to the displacement (d) and traction (t) boundary value problems, respectively. Then we can check whether the Betti's reciprocity theorem

$$\int_{\partial B} u_i^{(t)} t_i^{(d)} ds = \int_{\partial B} u_i^{(d)} t_i^{(t)} ds \tag{3.9}$$

is satisfied numerically within some acceptable accuracy.

ii) Perfect series and parallel systems are well known to result in the arithmetic and harmonic averages, or the so-called Voigt C^V and Reuss bounds C^R

$$C^V = f_1 C_1 + f_2 C_2 \quad C^R = \left(\frac{f_1}{C_1} + \frac{f_2}{C_2} \right)^{-1} \tag{3.10}$$

where f_1 and f_2 are the volume fractions of phases and 1 and 2, respectively.

iii) The case of small contrast in properties allows an expansion of, say, effective conductivity to second order in the difference $(C_2 - C_1)$ as follows [25]

$$C^{eff} = C_1 + f_2 (C_2 - C_1) - f_1 f_2 \frac{(C_2 - C_1)^2}{C_1} \frac{1}{d} + O(C_2 - C_1)^3 + \ldots \tag{3.11}$$

where d is the dimensionality of the space.

iv) There are many exact relations in the 2D conductivity. Perhaps the best well known one, due to [26] (also [27]) says that, for a two-phase isotropic system in 2D,

$$C^{eff}(C_1, C_2) C^{eff}(C_2, C_1) = C_1 C_2 \tag{3.12}$$

where $C^{eff}(C_1, C_2)$ is the effective conductivity of a given system, while $C^{eff}(C_1, C_2)$ is the effective conductivity with the phases 1 and 2 interchanged.

v) The CLM theorem [28,29] may be employed for planar elastic (classical as well as micropolar) simply connected inhomogeneous materials with twice differentiable properties. To this end, let us consider an effective compliance tensor S_{ijkl}^{eff} relating the volume averaged (denoted by overbar) stress and strain tensors

$$\overline{\varepsilon_{ij}} = S_{ijkl}^{eff} \overline{\sigma_{kl}}. \tag{3.13}$$

Now, the stresses σ_{11}, σ_{22} and σ_{12} are the same in the original and the equivalent materials $S_{ijkl}(\boldsymbol{x})$ and $S_{ijkl}^T(\boldsymbol{x})$, so that the strain fields ε_{ij} and ε_{ij} satisfy the relation

$$\begin{aligned} \overline{\varepsilon_{ij}} = S_{ijkl}^T \sigma_{kl} &= S_{ijkl} \sigma_{kl} + S_{ijkl}^I(\Lambda, -\Lambda) \sigma_{kl} \\ &= \varepsilon_{ij} + S_{ijkl}^I(\Lambda, -\Lambda) \sigma_{kl}. \end{aligned} \tag{3.14}$$

Here T stands for a transformed material. Carrying out the volume averaging of Eq. (3.14), and noting that $S_{ijkl}(\Lambda, -\Lambda)$ is independent of position $\boldsymbol{x}$, we find

$$\overline{\varepsilon_{ij}} = S_{ijkl}^{effT} \sigma_{kl} = S_{ijkl}^{eff} \overline{\sigma_{kl}} + S_{ijkl}^I(\Lambda, -\Lambda) \overline{\sigma_{kl}} \tag{3.15}$$

which shows that the effective compliance tensor of the second material is given by that of the first material plus the same shift as that for the individual phases

$$S_{ijkl}^{effT} = S_{ijkl}^{eff} + S_{ijkl}^I(\Lambda, -\Lambda). \tag{3.16}$$

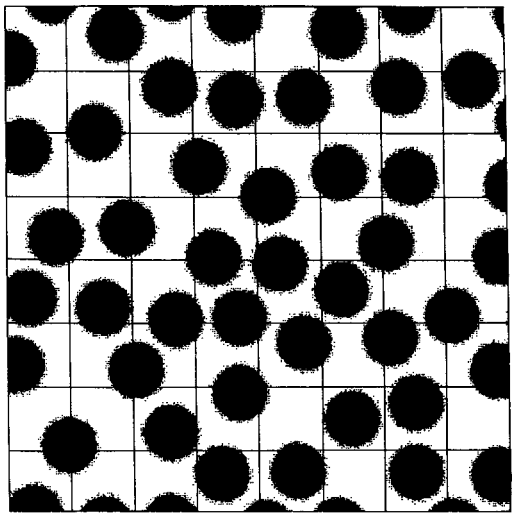

Fig. 9 A functionally graded matrix-inclusion composite with 47.2% volume fraction of black phase is partitioned into 8×8 subdomains, corresponding to a 64-processor parallel computer

When dealing with very large systems, the spring network method is limited by the available computer memory size. This is, for example, the case with a functionally graded material. A composite of that type is shown in Fig. 9, where the disk-matrix interphase is taken as a finite thickness zone of two randomly mixed phases of the disk (2) and the matrix (1) material. Both phases are locally homogeneous and isotropic—they are described by two constant isotropic conductivities C_1 and C_2. We see here three different length-scales: the fine structure of interphase region, the size and spacing of inclusions, and the macroscopic dimension of the composite.

For this type of problems, we can also use parallel computing. Thus, in Fig. 9 we show a partition of the entire simulated domain of a functionally graded composite into $64=8\times 8$ subdomains, each of which represents a 125×125 spring network that is assigned to a separate processor of a parallel computer. Thus, the boundary value is solved by using 64 processors operating in tandem. The computational effort is limited by the speed of a single processor (which goes down with the subdomain size) and the communication between the processors (which simultaneously goes up). Finding the optimal partition, is, therefore, an important task. There are, in principle, two ways to execute such a parallel scheme: either to write one's own software, or to adapt an existing solver running on a given parallel computer. The latter option is now becoming ever more realistic.

3.3 Example simulation of a polycrystal

The generalization of the Kirkwood spring network model outlined in Section 2 to an anisotropic case was motivated by a need to study micromechanics of a planar polycrystalline aluminum specimen [14]. The basic strategy is as follows. First, an image of crystal domains (*ie*, grains), such as the one showed in Fig. 10, needs to be scanned and mapped onto a triangular mesh. Next, every bond is assigned its stiffness depending on the domain it falls in. And finally, the mechanics problem of the resulting spring network is solved computationally.

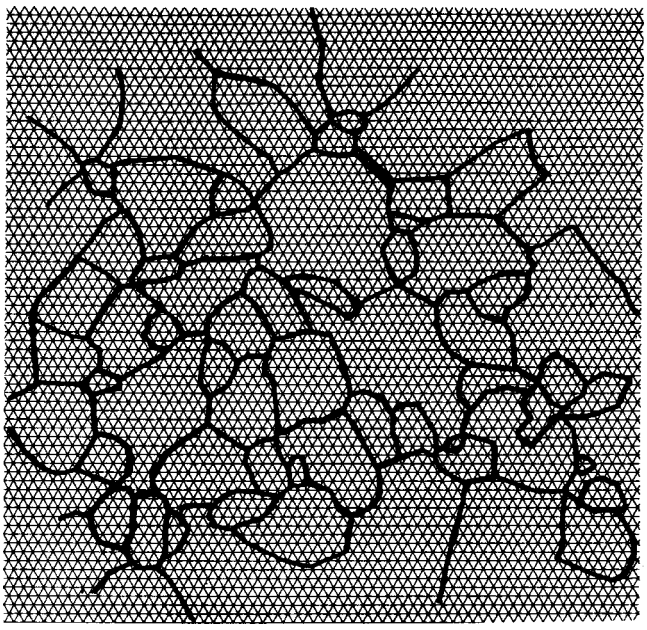

Fig. 10 Scanned image of a very thin polycrystal aluminum sheet. All the grain boundaries are orthogonal to the plane of the sheet

In order to assign spring stiffnesses to any node of the spring network mesh, the 3D stiffness tensor C_{ijkm} for each crystal must be found according to its transformation (rotation) matrix $a_{ij}\,(i,j=1,2,3)$; the latter is provided from the Kikuchi surface electron backscattering technique. Thus, to set up the spring network model, we start from the stiffness matrix $C_{\alpha\beta}$ of an (anisotropic) aluminum crystal which is given as

$$C_{\alpha\beta} = \begin{bmatrix} 10.82 & 6.13 & 6.13 & 0 & 0 & 0 \\ 6.13 & 10.82 & 6.13 & 0 & 0 & 0 \\ 6.13 & 6.13 & 10.82 & 0 & 0 & 0 \\ 0 & 0 & 0 & 2.85 & 0 & 0 \\ 0 & 0 & 0 & 0 & 2.85 & 0 \\ 0 & 0 & 0 & 0 & 0 & 2.85 \end{bmatrix} 10^4\text{MPa}. \tag{3.17}$$

Its fourth-rank stiffness tensor C_{ijkm} is then set up taking into account three symmetries $C_{ijkm}=C_{ijmk}=C_{jikm}=C_{kmij}$. We next use a transformation formula for a 4-th rank tensor

$$C'_{npqr}=a_{ni}a_{jp}a_{kq}a_{mr}C_{ijkm} \quad n,p,q,r=1,2,3 \tag{3.18}$$

to set up the in-plane part of C'_{npqr} at every mesh node. This 2D part, consisting of C'_{1111}, C'_{2222}, C'_{1122}, C'_{1112}, C'_{2212}, C'_{1212} is then mapped into the six spring constants α_1, α_2, α_3, β_1, β_2, β_3 according to Eq. (2.38). This mapping is one-to-one and is given as

$$\begin{bmatrix} C'_{1111} \\ C'_{2222} \\ C'_{1122} \\ C'_{1112} \\ C'_{1212} \\ C'_{2212} \end{bmatrix} = \begin{bmatrix} \frac{1}{\sqrt{3}} & \frac{1}{16\sqrt{3}} & \frac{1}{16\sqrt{3}} & \frac{\sqrt{3}}{4} & \sqrt{3} & \frac{\sqrt{3}}{4} \\ 0 & \frac{9}{16\sqrt{3}} & \frac{9}{16\sqrt{3}} & \frac{\sqrt{3}}{4} & \sqrt{3} & \frac{\sqrt{3}}{4} \\ 0 & \frac{\sqrt{3}}{16} & \frac{\sqrt{3}}{16} & -\frac{9}{4\sqrt{3}} & \frac{-\sqrt{3}}{2} & -\frac{\sqrt{3}}{4} \\ 0 & \frac{1}{16} & -\frac{1}{16} & \frac{3}{4} & 0 & -\frac{3}{4} \\ 0 & \frac{\sqrt{3}}{16} & \frac{\sqrt{3}}{16} & \frac{9}{4\sqrt{3}} & 0 & \frac{9}{4\sqrt{3}} \\ 0 & \frac{3}{16} & -\frac{3}{16} & -\frac{3}{4} & 0 & \frac{3}{4} \end{bmatrix} \times \begin{bmatrix} \alpha_1 \\ \alpha_2 \\ \alpha_3 \\ \beta_1 \\ \beta_2 \\ \beta_3 \end{bmatrix}. \tag{3.19}$$

While there was no ambiguity concerning the spring constant of any α-bond that entirely belonged to any given crystal domain, additional care had to be taken of the bonds that straddled the boundary of two crystals. The effective stiffnesses were assigned according to a series rule: $\alpha=(1/2\alpha_1+1/2\alpha_2)^{-1}$. Assignment of the β-springs, however, presented no such ambiguities. This lattice model offered a basis for study of intergranular multi-crack propagation in an elastic-brittle, thin (quasi-2D) aluminum sheet, that would otherwise require a very labor intensive task of finite element meshing and inter-element crack advance; see the aforementioned paper.

4 PLANAR SPRING NETWORKS ON PERIODIC LATTICES: NONCLASSICAL CONTINUA

4.1 Triangular lattice of Bernoulli-Euler beams

In the solid state physics literature, the Kirkwood and Keating models are sometimes referred to as the *beam-bending models*. This is a misnomer since there is no account taken in these models of the actual presence of moments and curvature change of spring bonds connecting the neighboring nodes. True beam bending was fully and rigorously considered by Wozniak [30] and his coworkers, and considering a limited access to that unique book, in this section we give a very brief account of the triangular lattice case.

We focus on the deformations of a typical beam, its bending into a curved arch allowing the definition of its curvature, and a cut in a free body diagram specifying the normal force F, the shear force $\tilde{F}$, and the bending moment M, see Fig. 11. It follows that in 2D, the force field within the beam network is described by fields of force-stresses σ_{kl} and moment-stresses m_k, so that, we have a micropolar medium.

The kinematics of a network of beams is now described by three functions

$$u_1(x) \quad u_2(x) \quad \varphi(x) \tag{4.1}$$

which coincide with the actual displacements (u_1, u_2) and rotations (φ) at the network nodes. Within each triangular pore, these functions may be assumed to be linear, and hence, the local strain, γ_{kl}, and curvature, κ_i, fields are related to u_1, u_2, and φ by

$$\gamma_{kl}=u_{l,k}+e_{lk}\varphi \quad \kappa_i=\varphi_{,i} \tag{4.2}$$

where e_{lk} is the Ricci symbol.

It follows from geometric considerations that

$$\gamma^{(b)}\equiv n_k^{(b)}n_l^{(b)}\gamma_{kl} \tag{4.3}$$

is the average axial strain, with $s^{(b)}\gamma^{(b)}$ being its average axial length change. Similarly,

$$\tilde{\gamma}^{(b)}\equiv n_k^{(b)}\tilde{n}_l^{(b)}\gamma_{kl}=n_k^{(b)}\tilde{n}_l^{(b)}u_{(l,k)}-\varphi \tag{4.4}$$

is the difference between the rotation angle of the beam chord and the rotation angle of its end node. Thus, the difference between the rotation angles of its ends is

$$\kappa^{(b)}\equiv n_k^{(b)}\kappa_k. \tag{4.5}$$

The elementary beam theory implies that the force-displacement and moment-rotation response laws of each bond (Fig. 11) are given as

$$F^{(b)}=E^{(b)}A^{(b)}\gamma^{(b)} \quad \tilde{F}^{(b)}=\frac{12E^{(b)}I^{(b)}}{s^2}\tilde{\gamma}^{(b)}$$

$$M^{(b)}=E^{(b)}I^{(b)}\kappa^{(b)} \tag{4.6}$$

where $A^{(b)}=wh$ is the beam cross-sectional area, $I^{(b)}=w^3h/12$ is its centroidal moment of inertia with respect to an axis normal to the plane of the network, and $E^{(b)}$ is the Young's modulus of the beam's material. All the beams are of length $s\equiv s^{(b)}$, which is the spacing of the mesh.

Turning now to the continuum picture, the strain energy of the micropolar continuum is expressed as

$$U_{continuum}=\frac{V}{2}\gamma_{ij}C_{ijkm}\gamma_{km}+\frac{V}{2}\kappa_i D_{ij}\kappa_j \tag{4.7}$$

from which we find

$$C_{ijkm}=\sum_{b=1}^{6}n_i^{(b)}n_k^{(b)}(n_j^{(b)}n_m^{(b)}R^{(b)}+n_j^{(b)}n_m^{(b)}\tilde{R}^{(b)})$$

$$D_{ij}=\sum_{b=1}^{6}n_i^{(b)}n_j^{(b)}S^{(b)} \tag{4.8}$$

where

$$R^{(b)}=\frac{2E^{(b)}A^{(b)}}{s^{(b)}\sqrt{3}} \quad \tilde{R}^{(b)}=\frac{24E^{(b)}I^{(b)}}{(s^{(b)})^3\sqrt{3}} \quad S^{(b)}=\frac{2E^{(b)}I^{(b)}}{s^{(b)}\sqrt{3}}. \tag{4.9}$$

If we assume all the beams to be the same ($R^{(b)}=R$, etc), we obtain

$$C_{1111}=C_{2222}=\tfrac{3}{8}(3R+\tilde{R}) \quad C_{1212}=\tfrac{3}{8}(R+3\tilde{R})$$

$$C_{1122}=C_{2211}=\tfrac{3}{8}(R-\tilde{R}) \quad C_{1221}=C_{2112}=\tfrac{3}{8}(R-\tilde{R})$$

$$D_{11}=D_{22}=\tfrac{3}{8}S \tag{4.10}$$

with all the other components of the stiffness tensors being zero. That is, we have

$$C_{ijkm}=\delta_{ij}\delta_{km}\Xi+\delta_{ik}\delta_{jm}\Lambda+\delta_{im}\delta_{jk}\Pi \quad D_{ij}^{\text{eff}}=\delta_{ij}\Gamma \tag{4.11}$$

in which

$$\Xi=\Pi=\tfrac{3}{8}(R-\tilde{R}) \quad \Lambda=\tfrac{3}{8}(R+3\tilde{R}) \quad \Gamma=\tfrac{3}{2}S. \tag{4.12}$$

We note from Eq. $(4.11)_1$ that this beam lattice is an isotropic continuum, rather than anisotropic as reported in [31,32].

The micropolar model [30,33] is conveniently expressed in terms of four compliances—*A*, *S*, *P*, and *M*—which are readily identified as

$$A=\frac{1}{\Xi+\dfrac{\Lambda+\Pi}{2}} \quad S=\frac{2}{\Lambda+\Pi} \quad P=\frac{2}{\Lambda-\Pi} \quad M=\frac{2}{3\Gamma}. \tag{4.13}$$

The effective bulk and shear moduli are now identified on the basis of Eq. (4.11) as

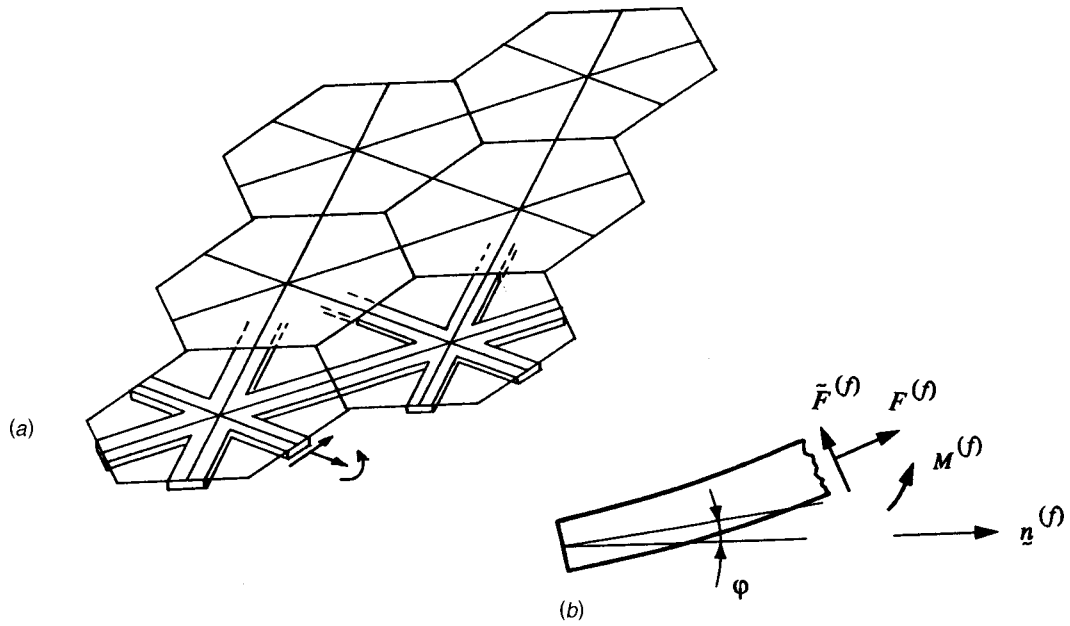

Fig. 11 The lattice geometry (a); curvature and internal loads in a single beam element (b)

$$\kappa = \tfrac{3}{4}R \quad \mu = \tfrac{3}{8}(R+\tilde{R}) \tag{4.14}$$

which are seen to reduce to the formulas of Section 2.3 in the special case of flexural rigidity being absent. Furthermore, the effective Young's modulus and Poisson's ratio are

$$E = 3R\frac{1+\dfrac{\tilde{R}}{R}}{3+\dfrac{\tilde{R}}{R}} \quad \nu = \frac{1-\dfrac{\tilde{R}}{R}}{3+\dfrac{\tilde{R}}{R}}. \tag{4.15}$$

It is noteworthy that the introduction of beam-type effects has a similar influence on E and ν as the introduction of the angular β-interactions in the Kirkwood model. However, noting that $\tilde{R}/R=(w/s)^2$, where w is the beam width, we see that, in view of the slenderness assumption of the beam elements, this model does not admit Poisson's ratios below ~ 0.2.

Finally, we note that the stiffness tensors (4.11) can be inverted to get the compliance tensors

$$S^{(1)}_{ijkm} = \tfrac{1}{4}[\,\delta_{ij}\delta_{km}(A-S)+\delta_{ik}\delta_{jm}(S+P)+\delta_{im}\delta_{jk}(S-P)]$$
$$S^{(2)}_{ij} = \frac{\delta_{ij}}{\Gamma} \tag{4.16}$$

so that, recalling the definition of the micropolar characteristic length [10],

$$l^2 = \frac{S+P}{4M} = \frac{l}{24}\,\frac{1+3\left(\dfrac{w}{s}\right)^2}{1+\left(\dfrac{w}{s}\right)^2} \tag{4.17}$$

where we used the basic facts relating the beam's cross-sectional area to its moment of inertia.

4.2 Triangular lattice of Timoshenko beams

In the foregoing section we began with the model of Bernoulli-Euler beams, which implies slender connections between the lattice nodes. It is well known that the situation of stubby connections is describable more adequately by Timoshenko beams. The boundary value problem that needs to be solved is that of a beam fixed at its both ends and subjected to a shear displacement at one end. That is, with the boundary conditions at the beam's left end

$$\nu(0)=0 \quad \theta(0)=0 \quad \nu'(0)-\theta(0)=0 \tag{4.18}$$

and right end

$$\nu(s)=\tilde{\gamma}^{(b)}s \quad \theta(s)=0 \quad \nu'(s)-\theta(s)=0 \tag{4.19}$$

it is readily determined from the beam's governing equations

$$E^{(b)}I^{(b)}\theta''+G^{(b)}A^{(b)}(\nu'-\theta)=0 \quad G^{(b)}A^{(b)}(\nu''-\theta')=0 \tag{4.20}$$

that a following relation holds between the shear force $\tilde{F}^{(b)}$ and the displacement $s\tilde{\gamma}^{(b)}$

$$\tilde{F}^{(b)} = \frac{12E^{(b)}I^{(b)}}{s^3(1+\beta)}\,s\tilde{\gamma}^{(b)}. \tag{4.21}$$

Here

$$\beta = \frac{12E^{(b)}I^{(b)}}{G^{(b)}A^{(b)}s^2} = \frac{E^{(b)}}{G^{(b)}}\left(\frac{w}{s}\right)^2 \tag{4.22}$$

is the dimensionless ratio of bending to shear stiffness, with $A^{(b)}=t_a w$ being the beam's cross-sectional area, and $I^{(b)}=t_a w^3/12$ its centroidal moment of inertia.

Two limiting cases of β are well known:
$\beta \to 0$, high shear stiffness and , hence, less deflection owing to shear; the Bernoulli-Euler slender beam is recovered;
$\beta > 1$, low shear stiffness and, hence, deflection owing to

shear dominates over that due to the Young's modulus $E^{(b)}$; this is the general case of the Timoshenko beam.

Observing that Eq. (4.21) replaces $(4.6)_2$, we now proceed to derive the effective moduli so that (4.9) is replaced by

$$R^{(b)}=\frac{2E^{(b)}A^{(b)}}{s^{(b)}\sqrt{3}} \quad \tilde{R}^{(b)}=\frac{24E^{(b)}I^{(b)}}{(s^{(b)})^3\sqrt{3}}\frac{1}{1+\beta}$$
$$S^{(b)}=\frac{2E^{(b)}I^{(b)}}{s^{(b)}\sqrt{3}} \tag{4.23}$$

wherein the ratio $\tilde{R}/R$ is

$$\frac{\tilde{R}}{R}=\left(\frac{w}{s}\right)^2\frac{1}{1+\beta}. \tag{4.24}$$

Following the same steps as in the previous section, we see that the effective continuum moduli are given by Eqs. (4.14)–(4.15) as before. It is now possible to express them in terms of the beam aspect ratio and β. Thus, for E^{eff} (normalized by the beam's modulus $E^{(b)}$) and ν^{eff}, we find

$$\frac{E^{\text{eff}}}{t_a E^{(b)}}=2\sqrt{3}\,\frac{w}{s}\,\frac{1+\left(\frac{w}{s}\right)^2\frac{1}{1+\beta}}{3+\left(\frac{w}{s}\right)^2\frac{1}{1+\beta}} \quad \nu^{\text{eff}}=\frac{1-\left(\frac{w}{s}\right)^2\frac{1}{1+\beta}}{3+\left(\frac{w}{2}\right)^2\frac{1}{1+\beta}}. \tag{4.25}$$

Considering the geometry of the hexagonal unit cell of the lattice, we can write the above in terms of the volume fraction of the material p (ie, unity minus the porosity)

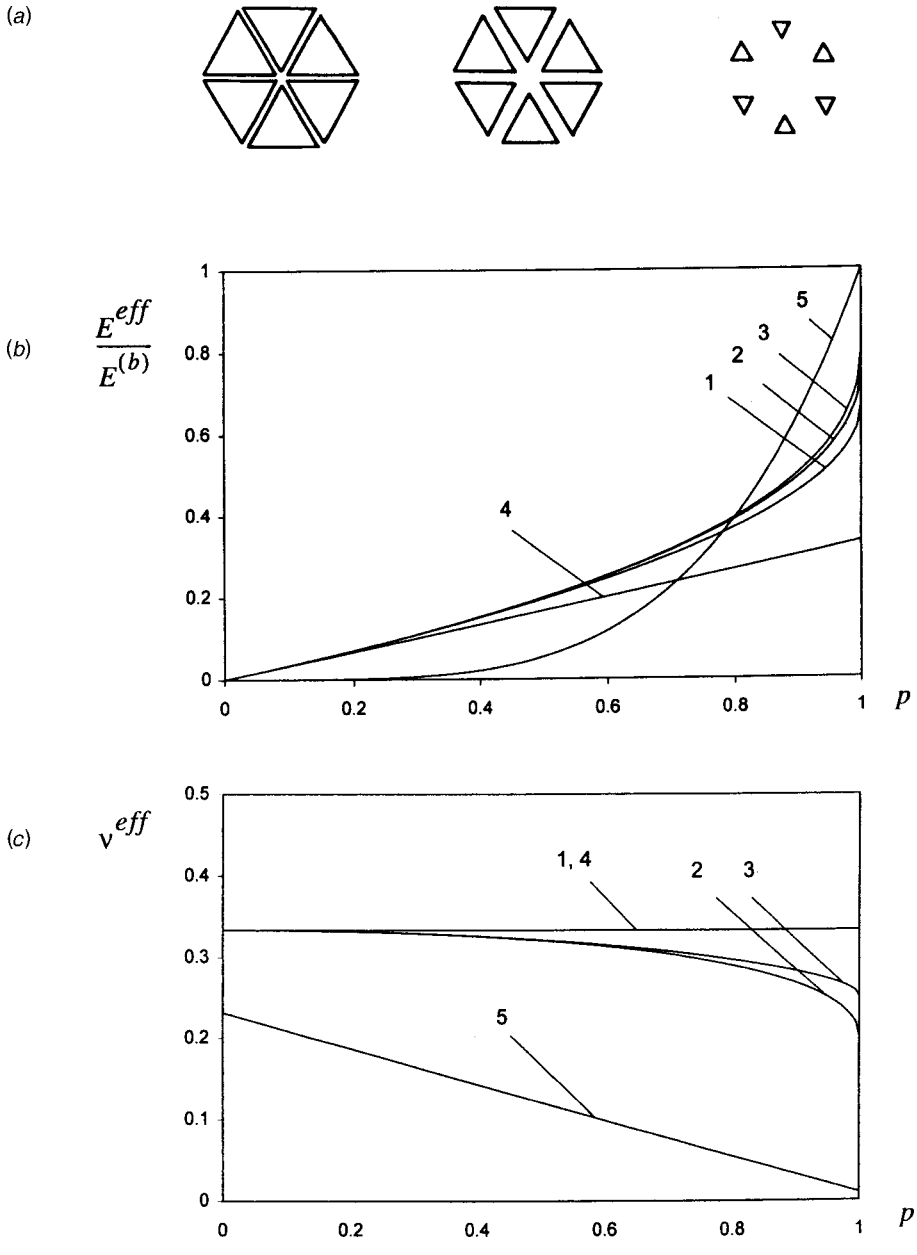

Fig. 12 *a*) A decrease in pore sizes (from left to right): from large holes (slender beams), through a lattice of stubby beams, to a plate perforated with small holes; shown at porosities $p=10\%$, 50%, and 90%-from right to left; *b*) The effective Young's modulus E^{eff}, normalized by the beam's Young's modulus $E^{(b)}$, as a function of p for: 1) the central-force lattice, 2) the Timoshenko beams lattice, 3) the Bernoulli-Euler beams lattice, 4) the Cox model, and 5) the effective medium theory for a perforated plate; and *c*) the effective Poisson's ratio ν^{eff} as a function of p, models (1–5) shown

$$\frac{E^{\text{eff}}}{t_a E^{(b)}} = 2(1-\sqrt{1-p})\,\frac{1+\dfrac{1}{3(1+\beta)}(1-\sqrt{1-p})^2}{3+\dfrac{1}{3(1+\beta)}(1-\sqrt{1-p})^2}$$

$$\nu^{\text{eff}} = \frac{3(1-\sqrt{1-p})^2\dfrac{3}{1+\beta}}{9+(1-\sqrt{1-p})^2\dfrac{3}{1+\beta}}. \tag{4.26}$$

The above are plotted in Fig. 12 *b*, *c* for the special case $E^{(b)}=9G^{(b)}$. We see that the consideration of lattice connections as stubby (Timoshenko) beams has a minor softening effect on E^{eff} relative to the Bernoulli-Euler beam model. This may be explained by noting that the admission of the beam's angle of rotation as an independent degree of freedom amounts to $G^{(b)}$ being finite, rather than infinite, in the Timoshenko beam model. The Poisson's ratio falls off nonlinearly from 1/3 with p increasing in both models. The admission of finite shear modulus is weak. Also plotted in Fig. 12 *b*, *c* are the results for the central-force lattice of Section 4.2, the perforated plate model introduced below, and the Cox model discussed in Section 5.

4.3 From stubby beams to a perforated plate model

As the volume fraction p rises beyond 50%, the beam's aspect ratio w/s increases so high that one can no longer model the connections between the lattice nodes as beams. Thus, a basic question arises: can any simple explicit model be derived for this low porosity range? One avenue is offered by a perforated plate model. In the limit of $p\to 1$, we have a plate with a regular distribution of triangular-shaped pores, Fig. 12*a*. This is a so-called *dilute limit* of a locally isotropic material with holes (in either periodic or disordered arrangements). Following [34,35], the respective formulas are

$$\frac{E^{\text{eff}}}{t_a E^{(b)}} = 1-\alpha(1-p) \qquad \nu^{\text{eff}} = \nu^{(b)} - \alpha(\nu^{(b)}-\nu_0)(1-p). \tag{4.27}$$

The coefficients $\alpha=4.2019$ and $\nu_0=0.2312$ have been computed in the above references, and, in fact, analogous coefficients are also available there for plates with other than triangular holes (squares, pentagons, ...). It is noteworthy that:

1) both formulas are uncoupled from one another;
2) $(4.27)_1$ models the low porosity range (high p-values) much better than the beam lattice model; summarizing, E^{eff} is modeled by an upper envelope of all the curves in Fig. 12*b*, *ie*, curves 3 and 5.
3) $(4.27)_2$ depends on the Poisson's ratio $\nu^{(b)}$ of the plate material; the latter can be specified only in the Timoshenko beam model.

One more question remains in connection with Fig. 12: What happens in the range of the p-values which are too high for a beam lattice model to hold and too low for the dilute model to be truly dilute? Or, can anything be done to smooth out the transition between the two curves 3 and 5 at p around 0.8? One could try here a usual device of micromechanics: an effective medium theory in any one of its guises: differential scheme, self-consistent, etc [35]. However, for the sake of clarity of Fig. 12*b*, *c*, we do not plot these.

Summing up, it is seen from Fig. 12 that, as p grows, beam bending tends to increase the effective Young's modulus E^{eff}. In other words, bending effects increase as connections become wider. On the other hand, as they become slender, one can work with segments carrying axial forces only. Thus, beam effects gain in influence as the pores' volume fraction decreases, and lead to an increase of the effective Young's modulus relative to the central-force model.

Two more things may be said about the beam network model. First, Timoshenko beams, although more sophisticated than Bernoulli-Euler beams, remain, in principle, 1D objects, of micropolar type, in fact. Therefore, what they yield is about as far as one can get with a beam model. A better approach should consider beam segments as little plates, *ie*, 2D objects, as recently implemented in [36]. Finally, lattice nodes that are taken as rigid objects in this model, could more realistically be modeled by considering their deformability; this will be demonstrated below.

4.4 Square lattice of Bernoulli-Euler beams

Following the same procedure as in Section 4.2, we now analyze a micropolar model of a square lattice network, Fig. 13; the triangular case was treated in [37]. Thus, assuming Bernoulli-Euler beams, we find an analogous version of Eq. (4.8)

$$C_{ijkm} = \sum_{b=1}^{4} n_i^{(b)} n_k^{(b)} (n_j^{(b)} n_m^{(b)} R^{(b)} + n_j^{(b)} n_m^{(b)} \tilde{R}^{(b)})$$

$$D_{ij} = \sum_{b=1}^{4} n_i^{(b)} n_j^{(b)} S^{(b)} \tag{4.28}$$

where

$$R^{(b)} = \frac{E^{(b)}A^{(b)}}{s^{(b)}} \quad \tilde{R}^{(b)} = \frac{12E^{(b)}I^{(b)}}{(s^{(b)})^3} \quad S^{(b)} = \frac{E^{(b)}I^{(b)}}{s^{(b)}}. \tag{4.29}$$

When all the beams are identical, this leads to

$$C_{1111}=C_{2222}=R \quad C_{1212}=C_{2121}=\tilde{R} \quad D_{11}=D_{22}=S \tag{4.30}$$

with all the other components of the stiffness tensors being zero. Clearly, this beam lattice results in a special case of an orthotropic continuum.

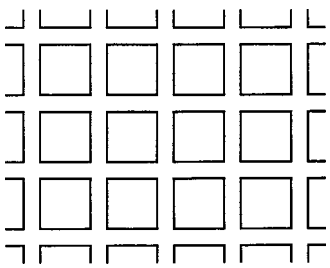

Fig. 13 A square beam lattice

In the foregoing derivation, lattice nodes were taken as rigid objects. As Wozniak [30] showed, this model may be generalized to a situation of deformable nodes, in which case we have

$$C_{ijkm}=\sum_{b=1}^{4}\left[n_i^{(b)}n_j^{(b)}\sum_{b_\perp=1}^{4}n_k^{(b)}n_m^{(b)}R^{(bb_\perp)}+n_i^{(b)}n_j^{(b)}n_k^{(b)}n_m^{(b)}\tilde{R}^{(b)}\right]$$

$$D_{ij}=\sum_{b=1}^{4}n_i^{(b)}n_j^{(b)}S^{(b)} \tag{4.31}$$

where

$$R^{(bb_\perp)}=\frac{d}{1-\nu_{(I)}\nu_{(II)}}\begin{bmatrix}\tilde{E}_{(I)} & \nu_{(I)}\tilde{E}_{(I)}\\ \nu_{(II)}\tilde{E}_{(II)} & \tilde{E}_{(II)}\end{bmatrix}$$

$$\tilde{R}^{(b)}=\frac{24E^{(b)}I^{(b)}}{(s^{(b)})^3\sqrt{3}}\quad S^{(b)}=\frac{2E^{(b)}I^{(b)}}{s^{(b)}\sqrt{3}} \tag{4.32}$$

Recently, an extension of such micropolar models—needed for wave propagation and vibration phenomena—has been carried out through the introduction of internal variables [38,39]. Such models, in contradistinction to the more classical homogenization methods, do more correctly account for the internal microstructure. For more recent work on models of lattice structures, see [40], and for mathematical aspects of their homogenization consult [41].

4.5 Non-local and gradient elasticity on a lattice with central interactions

Let us now focus our attention on a lattice made of two central force structures with: *structure I* (a regular triangular network with short range interactions) and *structure II* (three regular triangular networks with long-range interactions). These structures are superposed in a way shown in Fig. 14 so that a typical node communicates with its six nearest neighbors via structure I, and with its six second neighbors via structure II. Generalizing the development of Section 2.3, the central-force interaction in the spring connecting the nodes $\boldsymbol{r}$ and $\boldsymbol{r}'$ is related to the displacements $\boldsymbol{u}(\boldsymbol{r})$ and $\boldsymbol{u}(\boldsymbol{r}')$ of these nodes by

$$F_i(\boldsymbol{r},\boldsymbol{r}')=\Phi_{ij}^{\boldsymbol{r}\boldsymbol{r}'}\Delta u_j(\boldsymbol{r},\boldsymbol{r}') \tag{4.33}$$

where

$$\Phi_{ij}^{\boldsymbol{r}\boldsymbol{r}'}=\alpha^{\boldsymbol{r}\boldsymbol{r}'}\Delta r_i\Delta r_j\quad \Delta u_j(\boldsymbol{r},\boldsymbol{r}')=u_j(\boldsymbol{r}')-u_j(\boldsymbol{r})$$

$$\Delta r_i=r_i'-r_i\,. \tag{4.34}$$

Similar to the case of anti-plane elasticity, $\alpha^{\boldsymbol{r}\boldsymbol{r}'}$ is the spring constant of a half-length of a given interaction. However, assuming the structures I and II to be made of two types of springs, respectively, we simply have two kinds of spring constants: α^I and α^{II}. $s^I=2l$ is the lattice spacing of structure I, while $s^{II}=s^I\sqrt{3}$ is that of structure II.

A following question arises now: What continuum model should be set up to approximate this discrete system? Following [42], three types of continuum models will now be formulated: local, non-local, and strain-gradient.

a) Local continuum model

Proceeding as in Section 2.3 under conditions of uniform strain, and postulating the equivalence of strain energy in a unit cell of volume $V=2\sqrt{3}l$ due to all the spring constants

$$E=\frac{1}{2}\sum_{\boldsymbol{r},\boldsymbol{r}'}F_i(\boldsymbol{r},\boldsymbol{r}')\Delta u_i(\boldsymbol{r},\boldsymbol{r}')$$

$$=\frac{1}{2}\sum_{\boldsymbol{r},\boldsymbol{r}'}\Phi_{ij}^{\boldsymbol{r}\boldsymbol{r}'}\Delta u_i(\boldsymbol{r},\boldsymbol{r}')\Delta u_j(\boldsymbol{r},\boldsymbol{r}') \tag{4.35}$$

to equal the strain energy of an effective continuum

$$E_{continuujm}=\frac{1}{2}\int_V\varepsilon_{ij}C_{ijkm}\varepsilon_{km}dV \tag{4.36}$$

we determine an effective, local-type stiffness tensor

$$C_{ijkm}=C_{ijkm}^I+C_{ijkm}^{II} \tag{4.37}$$

where

$$C_{ijkm}^I=\frac{2}{\sqrt{3}}\alpha^I\sum_{b=1,2,3}n_i^{I(b)}n_j^{I(b)}n_k^{I(b)}n_m^{I(b)}$$

$$C_{ijkm}^{II}=\frac{6}{\sqrt{3}}\alpha^{II}\sum_{b=1,2,3}n_i^{II(b)}n_j^{II(b)}n_k^{II(b)}n_m^{II(b)}\,. \tag{4.38}$$

The $n_i^{I(b)}$ and $n_i^{II(b)}$ are given by Eq. (2.20). The above tensors are of the form (2.25), so that

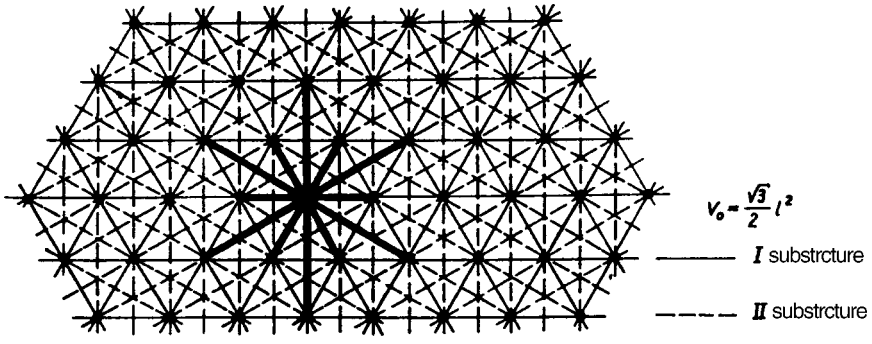

Fig. 14 Two structures, I and II, resulting in a lattice with local (nearest neighbor) and nonlocal (second neighbor) interactions. Note that the structure II consists of three triangular networks having separate sets of nodes, and that all these nodes coincide with the nodes of structure I.

$$\lambda^I=\mu^I=\frac{3}{4\sqrt{3}}\alpha^I \quad \lambda^{II}=\mu^I=\frac{3}{4\sqrt{3}}\alpha^{II} \tag{4.39}$$

b) Non-local continuum model

A non-local model should result in stresses at a point dependent upon the deformation within the range of interactions associated with the point. As a result, the more inhomogeneous is the strain field, the closer is the non-local model to grasping the actual strain state of the lattice. First, we distribute the values of tensors C^I_{ijkm} and C^{II}_{ijkm} at point $\boldsymbol{r}$ uniformly over the regions of interactions of structures I and II (Fig. 14), and form a new tensor $C_{ijkm}(\boldsymbol{r},\boldsymbol{r}')$ such that

$$C_{ijkm}(\boldsymbol{r},\boldsymbol{r}')=C^I_{ijkm}(\boldsymbol{r},\boldsymbol{r}')+C^{II}_{ijkm}(\boldsymbol{r},\boldsymbol{r}')$$

$$C^I_{ijkm}(\boldsymbol{r},\boldsymbol{r}')=\frac{C^I_{ijkm}h^I(\boldsymbol{r},\boldsymbol{r}')}{A^I}$$

$$C^{II}_{ijkm}(\boldsymbol{r},\boldsymbol{r}')=\frac{C^{II}_{ijkm}h^{II}(\boldsymbol{r},\boldsymbol{r}')}{A^{II}} \tag{4.40}$$

Here $A^I=\pi(s^I)^2$, $A^{II}=\pi(s^{II})^2$ are the areas, while $h^I(\boldsymbol{r},\boldsymbol{r}')$ and $h^{II}(\boldsymbol{r},\boldsymbol{r}')$ are the characteristic functions of the regions of interactions in the neighborhood of $\boldsymbol{r}$.

c) Strain-gradient continuum model

A strain-gradient model is similar to the non-local model in that it resolves the local inhomogeneity of deformation within the range of interactions associated with a continuum point. One begins here with a series expansion of the relative displacement field involving two terms—linear and quadratic—that is

$$\Delta u_j(\boldsymbol{r},\boldsymbol{r}')=\varepsilon^{\boldsymbol{r}}_{ij}(r'_j-r_j)+\tfrac{1}{2}\gamma^{\boldsymbol{r}}_{ijk}(r'_j-r_j)(r'_k-r_k) \tag{4.41}$$

where

$$\varepsilon^{\boldsymbol{r}}_{ij}=u_{(i,j)}(\boldsymbol{r}) \quad \gamma^{\boldsymbol{r}}_{ijk}=\varepsilon_{(i,j,k)}(\boldsymbol{r}) \tag{4.42}$$

are gradients of the first and second orders, respectively, of the displacement field.

In view of Eq. (4.43), the elastic energy of the structure (4.37) is now expressed as

$$E=\frac{1}{2}\sum_{\boldsymbol{r},\boldsymbol{r}'}\Phi^{\boldsymbol{r}\boldsymbol{r}'}_{ij}\left[\varepsilon^{\boldsymbol{r}}_{ik}(r'_k-r_k)+\frac{1}{2}\gamma^{\boldsymbol{r}}_{ikm}(r'_k-r_k)(r'_m-r_m)\right]$$
$$+[\varepsilon^{\boldsymbol{r}}_{jm}(r'_m-r_m)+\tfrac{1}{2}\gamma^{\boldsymbol{r}}_{jmn}(r'_m-r_m)(r'_n-r_m)]. \tag{4.43}$$

Noting the continuum form of energy

$$E_{\text{continuum}}=\frac{1}{2}\int_V(\varepsilon_{ij}C_{ijkl}\varepsilon_{kl}+\gamma_{ijk}C_{ijklmn}\gamma_{lmn})dV \tag{4.44}$$

one can identify

$$C_{ijkl}(\boldsymbol{r},\boldsymbol{r}')=C^I_{ijkl}(\boldsymbol{r},\boldsymbol{r}')+C^{II}_{ijkl}(\boldsymbol{r},\boldsymbol{r}')$$

$$C_{ijklmn}(\boldsymbol{r},\boldsymbol{r}')=C^I_{ijklmn}(\boldsymbol{r},\boldsymbol{r}')+C^{II}_{ijklmn}(\boldsymbol{r},\boldsymbol{r}') \tag{4.45}$$

where

$$C^I_{ijkl}(\boldsymbol{r},\boldsymbol{r}')=\frac{2E^IA^I}{\sqrt{3}s^I}\sum_{b=1,2,3}n^{I(b)}_in^{I(b)}_jn^{I(b)}_kn^{I(b)}_l$$

$$C^I_{ijklmn}(\boldsymbol{r},\boldsymbol{r}')=\frac{2E^IA^Is^I}{\sqrt{3}}\sum_{b=1,2,3,}n^{I(b)}_in^{I(b)}_jn^{I(b)}_kn^{I(b)}_ln^{I(b)}_mn^{I(b)}_n \tag{4.46}$$

with completely analogous formulas holding for $C^{II}_{ijkl}(\boldsymbol{r},\boldsymbol{r}')$ and $C^{II}_{ijklmn}(\boldsymbol{r},\boldsymbol{r}')$. Further considerations of these models, especially in connection with the setup of boundary value problems, the modeling of surface energy accounting for the heterogeneity of material properties in the boundary layer of the microstructure, and the determination of the internal forces are given in [43]. The subject of higher order gradient theories has received a lot of attention over the last decade, eg, [44].

4.6 Plate-bending response

We can apply the same approach as that outlined so far for the in-plane problems, to the determination of effective plate-bending response of a periodic beam network. We sketch the basic ideas in terms of a triangular lattice, within the assumptions of a Kirchhoff (thin) plate model. To this end, we must consider out-of-plane deformations of a triangular geometry lattice, Fig. 15. The kinematics is, therefore, described by three functions—one out-of-plane displacement and two rotations (with respect to the x_1 and x_2 axes)

$$u(\underset{\sim}{x}) \quad \varphi_1(\underset{\sim}{x}) \quad >\varphi_2(\underset{\sim}{x}) \tag{4.47}$$

which coincide with the actual displacement (u) and rotations (φ_1,φ_2) at the lattice vertices. Within each triangular pore these functions may be assumed to be linear. It follows then that the strain and curvature fields are related to u, φ_1, φ_2 by

$$\kappa_{kl}=\varphi_{l,k} \quad \gamma_k=u_{,k}+\varepsilon_{kl}\varphi_l. \tag{4.48}$$

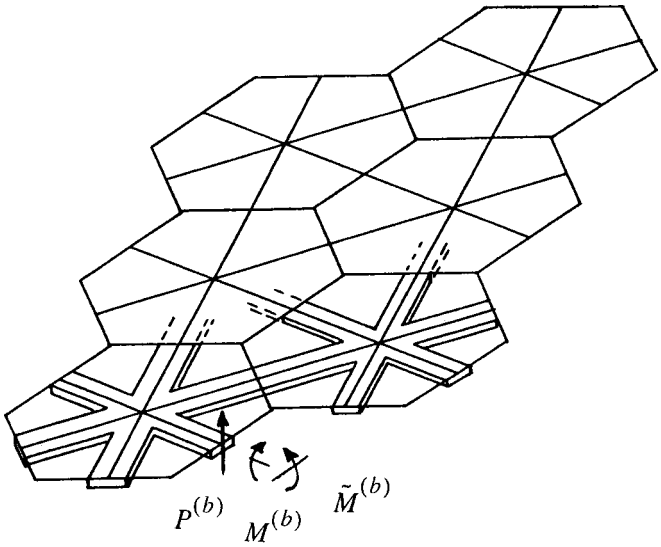

Fig. 15 A perspective view of a triangular geometry lattice, showing the relevant internal loads in a beam cross section

With reference to Fig. 15, the mechanical (force-displacement and moment-rotation) response laws of each beam are given as

$$M^{(b)}=C^{(b)}\kappa^{(b)} \quad \tilde{M}^{(b)}=E^{(b)}I^{(b)}\tilde{\kappa}^{(b)}$$

$$P^{(b)}=\frac{12E^{(b)}I^{(b)}}{s^{(b)}}\tilde{\gamma}^{(b)} \tag{4.49}$$

where $A^{(b)}=t_a w$ is a cross-sectional area of the beam; $I^{(b)}=t_a^3 w/12$ is a centroidal moment of inertia of the cross-sectional area of the beam with respect to an axis normal to the plane of the lattice; $s^{(b)}=2l^{(b)}$ is the full length of each beam. The mechanical quantities are as follows: $C^{(b)}$ is a torsional stiffness of the beam; $E^{(b)}$ is Young's modulus of the beam; $M^{(b)}$ is an in-plane twisting moment in the beam; $\tilde{M}^{(b)}$ is an out-of-plane bending moment in the beam; $P^{(b)}$ is a shear force in the beam; $\tilde{\gamma}^{(b)}$ is a beam shear deformation; and $\kappa^{(b)}$ is a beam's curvature.

The strain energy of the unit cell is

$$U_{continuum}=\frac{V}{2}\overline{\kappa}_{ij}C^{eff}_{ijkl}\overline{\kappa}_{kl}+\frac{V}{2}\overline{\gamma}_i A^{eff}_{ij}\overline{\gamma}_j \tag{4.50}$$

which is consistent with the Hooke's law

$$m_{kl}=C_{ijkl}\kappa_{kl} \quad p_k=A_{kl}\gamma_l . \tag{4.51}$$

Here m_{kl} is the tensor of moment-stresses, p_k is the vector of shear tractions.

Proceeding in a fashion analogous to the in-plane problems, Wozniak [30] found

$$C^{eff}_{ijkl}=\sum_{b=1}^{6} n_i^{(b)}n_k^{(b)}(n_j^{(b)}n_l^{(b)}S^{(b)}+n_j^{(b)}n_l^{(b)}\tilde{S}^{(b)})$$

$$A^{eff}_{ij}=\sum_{b=1}^{6} n_i^{(b)}n_j^{(b)}R^{(b)} \tag{4.52}$$

where

$$S^{(b)}=\frac{C^{(b)}}{s^{(b)}} \quad \tilde{S}^{(b)}=\frac{E^{(b)}I^{(b)}}{s^{(b)}} \quad \hat{R}^{(b)}=\frac{12E^{(b)}I^{(b)}}{\tilde{s}^{(b)}(s^{(b)})^2} \tag{4.53}$$

In the case of a triangular lattice made of identical beams ($E^{(b)}=E$, etc), we find

$$C_{ijkl}=\delta_{ij}\delta_{kl}\Delta+\delta_{ik}\delta_{jl}Y+\delta_{il}\delta_{jk}\Omega \quad A_{ij}=\delta_{ij}B \tag{4.54}$$

in which

$$\Delta=\Omega=\tfrac{3}{8}(S-\tilde{S}) \quad Y=\tfrac{3}{8}(S+3\tilde{S}) \quad B=\tfrac{3}{2}\hat{R}$$

$$S=\frac{2C}{s\sqrt{3}} \quad \tilde{S}=\frac{2EI}{s\sqrt{3}} \quad \hat{R}=\frac{24EI}{s^3\sqrt{3}}. \tag{4.55}$$

Same type of derivation may be conducted for a lattice of rectangular geometry.

4.7 Honeycomb lattice of Timoshenko beams

Recent years have seen a growing activity in mechanics of foams and porous media. Here, a generic model is provided by a honeycomb lattice of beams. By analyzing the rhombus-shaped cell of Fig. 5*a* with hexagons of side length *s*, Wang and Stronge [45] derived a micropolar model with the energy of unit cell in the form (4.7). In particular, the non-zero members of stiffness tensors C_{ijkm} and D_{ij} were found as

$$C_{1111}=C_{2222}=\frac{s\sqrt{3}}{4wE}\left[\left(\frac{s}{w}\right)^2+3\right]$$

$$C_{1122}=C_{2211}=\frac{s\sqrt{3}}{4wE}\left[1-\left(\frac{s}{w}\right)^2\right]$$

$$C_{1212}=C_{2121}=\frac{s\sqrt{3}}{4wE}\left[3\left(\frac{s}{w}\right)^2+1\right]$$

$$C_{1221}=C_{2112}=\frac{s\sqrt{3}}{4wE}\left[1-\left(\frac{s}{w}\right)^2\right]$$

$$D_{11}=D_{22}=\frac{12\sqrt{3}}{E}\left(\frac{s}{w}\right)^3 \tag{4.56}$$

where $E\equiv E^{(b)}$. Clearly, this beam lattice results in an isotropic continuum, and we note (recall Appendix again) that its effective Poisson's ratio is about unity.

We refer the reader to [46] for continuum-type fracture analyses of porous materials with hexagonal as well as square and triangular microgeometries.

5 RIGIDITY OF NETWORKS

5.1 Structural topology and rigidity percolation

When considering a central force (or truss) system, a question of fundamental importance is whether such a structure is a sufficiently constrained system or not. In other words, is it an intrinsically rigid body? This is the subject matter of a field called *structural topology*. In the following, we provide its basic concepts. Any central force network is a set of vertices bars, or edges, and nodes (frictionless pivots), or vertices. We immediately have an edge set E, and a vertex set V, so that the network is represented by a graph $G(V,E)$. An edge is an unordered pair of two vertices. Structural rigidity can be based on statics or on kinematics, and, as we shall see below, they are in a certain sense equivalent.

The statical approach involves, in the first place, the concept of an equilibrium load. A system of forces assigned to the nodes of a network is said to be an *equilibrium load* if and only if (*iff*) the sum of the assigned vectors is the zero vector, and the total moment of those vectors about any one point is zero. A network resolves an equilibrium load *iff* there is an assignment of tensions and compressions to all the bars of E, such that the sum at each node is equal and opposite to its assigned load. A structure is said to be statically rigid *iff* it resolves all equilibrium loads.

The kinematical approach involves the concept of an infinitesimal motion, which is an assignment of velocities to all the nodes of V, such that the difference of velocities assigned to the ends of any bar is perpendicular to the bar itself. This means that the motion does not result in any extension or compression of the bar. Every connected plane structure has at least three degrees of freedom (two translations and one rotation), and this is called a *rigid motion*. A

structure is said to be *infinitesimally rigid iff* all its infinitesimal motions are rigid motions. These statical and kinematical pictures are connected by a theorem due to Crapo and Whiteley [47]: A structure is statically rigid *iff* it is infinitesimally rigid.

A structure is said to be *isostatic iff* it is minimally rigid, that is, when it is infinitesimally rigid. But, the removal of any bar introduces some infinitesimal motion. Clearly, in an isostatic structure all the bars are necessary to maintain the overall rigidity. In statics, this is called a statically determinate structure, as opposed to the indeterminate ones which have more than a minimally sufficient number of bars for the global rigidity. It is a well known result that, in 2D, a determinate structure of $|V|$ nodes has edges numbering

$$|E|=2|V|-3 \tag{5.1}$$

where $|\ |$ denotes the number of elements in a given set. As an example, let us consider an incomplete triangular lattice shown in Fig. 16. While it satisfies Eq. (5.1), it is not at all clear whether it is isostatic.

This example shows that $|E|=2|V|-3$ is only a necessary, but not a sufficient condition for rigidity. The latter is provided by this theorem (eg, [48,49]): A planar graph structure is isostatic if and only if it has $2|V|-3$ bars, and for every m, $2\leqslant m\leqslant|V|$, no subset of m nodes has more than $2m-3$ bars connecting it. This, effectively, allows one to check whether the edges of the graph are not distributed spatially in a uniform manner. If they are crowded locally, than the odds are that the structure is not isostatic.

The isostatic concept so far discussed falls in the category of generic rigidity, where only the topological information on a graph's connectivity comes into picture. However, one may also deal with the unexpected infinitesimal motions when, say, two edges incident onto the same vertex lie on a straight line. When dealing with very large systems—as encountered in condensed matter physics—we need to ask the question: What critical fraction, p_r, of edges of E needs to be kept so as to render the structure isostatic? We note that we would have $|E'|=p_r|E|$ new edges of thus modified, or depleted, set $|E'|$. It follows immediately from $|E'|=2|V|-3$ that we would have $p_r=2/3$. This value is a simple estimate of the so-called *rigidity percolation*, a concept also useful in condensed matter and biophysics, eg [50–52]. As shown in these references, the actual critical point occurs at a little different value than 2/3; theoretical methods involved include effective medium theories and spring network computations. The latter of these will be demonstrated later on the example of Delaunay networks.

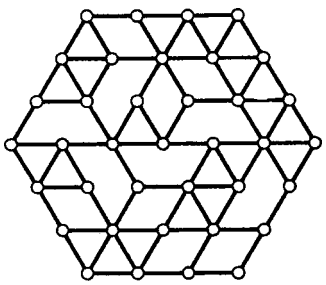

Fig. 16 A triangular lattice with 71 edges and 37 vertices; it is generically rigid.

Finally, it is important to keep in mind that the rigidity percolation typically occurs above the connectivity percolation, ie, $p_r>p_c$. For example, p_c for a triangular network equals 1/3.

5.2 Rigidity of a graph of Poisson line field geometry

The Poisson line field [53] forms a classical model of a cellulose fiber network encountered in paper [54]. We now identify the line segments (between any two consecutive intersections) to be edges of E, and pivots to be vertices of V. Let us recall that the triple-fiber intersections occur with probability zero for isotropic and anisotropic distributions of lines angles. Thus, we typically have vertices of connectivity 4, *ie*, V_4.

Now, with reference to Fig. 17*a*, which shows a typical realization of the Poisson line field, we see that there are two types of edges: those in direct contact with the square shaped window, and those entirely in the interior. Clearly, the square window is needed to prevent these boundary layer bonds from dangling, and this immediately renders the entire

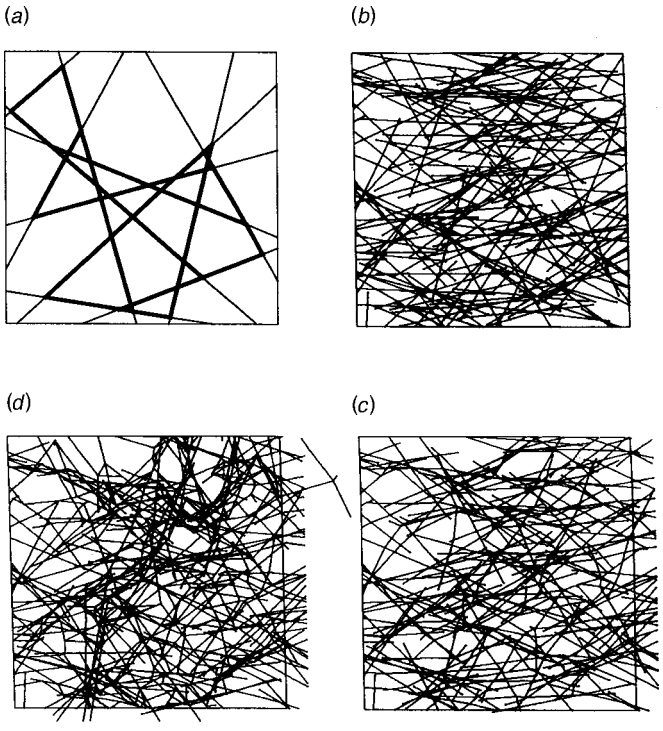

Fig. 17 Samples of *a*) a planar Poisson line field and *b*) a finite fiber field generated from (5.4) with $a_1=1$ and all other a_i's equal zero. Test windows of size $L\times L$ are considered. *c*) Deformation of a network of (b), with 195 fibers at a preference in the x_1-direction at $\delta=2$ with originally straight fibers, with fiber bending present, subjected to axial strain $\epsilon_{11}=1\%$. *d*) The same network, with fiber bending almost absent, subjected to axial strain $\epsilon_{11}=1\%$. All displacements in *c*) and *d*) are magnified by a factor 8 for clarity. Figure *d*) shows large, mechanism-type motions of the network including those of some fibers which spring outside the original domain of the network.

network a mechanism. However, one may argue that the boundary layer of dangling bonds is very thin relative to the whole field, and ask the question concerning the isostatic condition for the graph $G(V,E)$ representing the interior network of edges not directly in contact with the square window boundary; these are shown in bold in Fig. 17*a*. Here we observe that, while the V_4 vertices occur in the interior of this graph, its boundary involves V_2 and V_3 vertices. Now, since there are two vertices to every edge, we can calculate the total number of edges in the bold drawn graph $G(V,E)$ according to

$$|E|=|V^2|+\tfrac{3}{2}|V_3|+2|V_4| \tag{5.2}$$

Evidently, since $V=V_2\cup V_3\cup V_4$, the total number of all the vertices is

$$|V|=|V_2|+|V_3|+|V_4| \tag{5.3}$$

so that $|E|<2|V|-3$. The system is not isostatic, it is underconstrained (ie, a mechanism). Given this observation, the Poisson line field of axial force fiber segments (the so-called Cox model [54]) is not a valid model of paper or any other solid material for that matter. The fact that the Cox model does give finite values for elastic moduli including the shear modulus, is easily explained by the presence of fully stretched fibers spanning the entire test window. The situation is analogous to a graph of a square lattice topology, which, even though it is an obvious mechanism, will give finite axial moduli in two directions if fully stretched and subjected to kinematic boundary conditions.

In real networks, fibers have finite length, so their ends are loose. When fiber ends are removed to eliminate their obvious mechanism motions, the number of vertices in sets V_2 and V_3 increases. Consequently, Eq. (5.1) is even further from being satisfied. In order to deal with finite fiber effects, Cox and others modified the basic model by a so-called shear-lag theory. However, the latter assumes single fiber segments to carry axial and shear forces only, which (see Section 6), is not a valid model of a solid element: fiber bending should also be included.

Paper exhibits finite stiffnesses in 2D as well as in 3D. In the latter case, condition (5.1) is replaced by an even more stringent one as more constraints are needed when dealing with the additional degrees of freedom [49].

5.3 Loss of rigidity in a fiber-beam network

Besides the foregoing structural topology considerations, there is another fact which casts doubt on any fiber network model in which fiber segments are joined by pivots. Namely, any two cellulosic fibers have a finite contact area of hydrogen bonding [55], which would be sheared by hinge-type connections. While it is very difficult to assess experimentally to what extent this region is deformable, our model will treat it as somewhat deformable in the sense that bonds are rigid, but have no dimension, and fiber segments are treated as extensible beams from node to node of the graph $G(V,E)$ [56]. This modeling of mechanics of fiber networks is similar to that of *i*) cement-coated wood strands composites [57], *ii*) highly porous materials [58], and *iii*) battery systems [59,60]. In general, it is based on the following assumptions and steps:

1) Generate a system of finite-length straight fibers such as shown in Fig. 17*b* according to specific geometric characteristics: distribution of fiber lengths and widths, distribution of angular orientations of fiber chords, etc. The fibers are laid in three dimensions on top of one another with a possible non-zero out-of-plane angle according to a Fourier series-type probability density function

$$p(\theta)=\frac{1}{\pi}(1+a_1\cos 2\theta+a_2\cos 4\theta+\ldots +a_n\cos 2n\theta+\ldots)\quad 0<\theta\leqslant\pi \tag{5.4}$$

θ is the angle a fiber makes with respect to the *x*-axis, and it must be between zero and π.
2) Fibers are homogeneous, but each fiber may have different dimensions and mechanical properties, all sampled from any prescribed statistical distribution.
3) Each fiber is a series of linear elastic 3D extensible Timoshenko beam elements. Each of these is described by a stiffness matrix written here in an abbreviated form set up in a corotational coordinate system [61]

$$\begin{bmatrix} F\\ T\\ M_y^a\\ M_z^a\\ M_y^b\\ M_z^b \end{bmatrix}=\begin{bmatrix} \frac{EA}{l} & 0 & 0 & 0 & 0 & 0\\ 0 & \frac{GJ}{l} & 0 & 0 & 0 & 0\\ 0 & 0 & 4a(l^2+3g) & 0 & 2a(l^2-6g) & 0\\ 0 & 0 & 0 & 4b(l^2+3h) & 0 & 2b(l^2-6h)\\ 0 & 0 & 2a(l^2-6h) & 0 & 4a(l^2+3g) & 0\\ 0 & 0 & 0 & 2b(l^2-6h) & 0 & 4a(l^2+3g) \end{bmatrix}\begin{bmatrix} \Delta L\\ \Delta\theta_x\\ \theta_y^a\\ \theta_z^a\\ \theta_y^b\\ \theta_z^b \end{bmatrix} \tag{5.5}$$

where

$$g=12\frac{EI_y}{GA}\quad h=12\frac{EI_z}{GA}\quad a=\frac{EI_y}{l(12g+l^2)}\quad b=\frac{EI_z}{l(12h+l^2)}. \tag{5.6}$$

Here F and T are the axial force and the twisting moment, while M_y^a, M_z^a, M_y^b, and M_y^b, are the bending moments around the y and z axes at the a and b ends, respectively. Also, ΔL, $\Delta\theta_x$, θ_y^a, θ_z^a, θ_y^b, and θ_z^b denote axial elongation, angle of twist, and four angles of rotation. Finally, l, A, J, I_x, and I_y are, respectively, the length, cross-sectional area, cross-sectional polar moment of inertia, and the moments of inertia with respect to the x and y axes. E and G are the Young's modulus and shear modulus of a fiber

4) All the intersection points are identified so as to set up a connectivity matrix.
5) Equilibrium is found under kinematic boundary conditions $u_i=\overline{\epsilon}_{ij}x_j$.
6) All six effective, in-plane stiffness coefficients are determined from the postulate of equivalence of strain energy stored in a square-shaped window of finite thickness with the strain energy of an equivalent, hypothetical continuum.

The undeformed network, shown in Fig. 17*b* in its top view, has the following parameters: window size: $4\times4\times0.1$ mm $a_1=1$, and other coefficients in Eq. (5.4) are zero; fiber length: 2 mm; fiber width : 0.04 mm; fiber height: 0.015 mm. As a result of a Boolean process of fiber placement (eg, [62]), we obtain: 195 fibers with an average of 4.8 bonds per fiber, the whole system having 859 nodes with six degrees of freedom per node.

A state of deformation corresponding to axial strain $\epsilon_{11}=8\%$ is shown in Fig. 17*c*. The analyzed strain is actually 1%, and displacements are magnified for clarity. Compare this deformed network to that in Fig. 17*d*, which shows the same network of fibers subjected to the same strain but with the ratio of fiber flexural stiffness to fiber axial stiffness reduced by a factor of 10^{-4}. Note the following:

1) The sharp kinks we see in both figures are only the artifact of simple computer graphics—the micromechanical model assumes fibers deform into differentiable curves. Magnification creates the appearance of large displacements. Actually, an infinitesimal displacement assumption is used in the computational mechanics program.
2) The kinks are far more pronounced when fibers have low flexural stiffness. Portions of the network where connected fibers do not form triangular pores can generate significant forces in response to deformation when fibers have high flexural stiffness, but they cannot do so when fibers rely almost entirely on axial stiffness. These portions of the network are not stable in the sense of loss of generic rigidity discussed earlier.
3) We do not study this rigid-floppy transition by turning, in an *ad hoc* fashion, all the connections into pivots. Rather, with the model taking into account all the displacements and rotations of nodes, we can study it as a continuous function of fiber slenderness; see also [63]. Note that this aspect is impossible to investigate with models based on central-force potentials for single fiber segments [64]. Our model, thus, fills the gap pointed out in [65] consisting of a need to set up finite element models of 3D disordered fiber networks, yet avoids their simplistic mapping into electrical resistor networks of the same topology.
4) The network of fiber-beams, together with a two-scale geometric disorder, offers a possible explanation of the special orthotropy of paper in which the shear modulus is effectively invariant with respect to rotations [66].

6 SPRING NETWORK MODELS: DISORDERED TOPOLOGIES

6.1 Load transfer mechanisms in heterogeneous media

The spring network models are most natural when applied to systems that have the same topology as the underlying lattice. One instinctive example has been discussed in Section 4.5: a cellulose fiber network. Another one is offered by a granular medium. Here, the principal method of computational mechanics analyses, dating back to [67], is called the *discrete element* (DE) *model*.

Let us here employ a graph representation of the planar granular medium: a graph $G(V,E)$, whereby vertices of the set V signify grain centers and edges of the set E represent the existing grain-grain interactions, Fig. 18(*a*). We fix an r-θ polar coordinate system at a grain's center. There are several types of the DE model that one may consider.

- Central interactions: the total energy is a sum total of central interactions of all the edges
$$U=U^{\text{central}} \tag{6.1}$$
and this model is a generalization of the basic model of Section 2.3.
- Central and angular interactions: the total energy is modified to
$$U=U^{\text{central}}+U^{\text{angular}} \tag{6.2}$$
and, this model is a generalization of what we saw in Section 2.4. Continuum mechanics tells us that $\epsilon_{\theta\theta}$ equals $\partial r^{-1}u\theta/\partial\theta+u_r/r$. This shows that the angular changes $\Delta\phi/\phi$ between two adjacent edges V_1-V_2 and V_1-V_3 in Fig. 18 correspond to $\partial r^{-1}u\theta/\partial\theta$ in the r-θ polar coordinate system fixed at a grain's center. This term does not show up in two other expressions for ϵ_{rr} and $\epsilon_{r\theta}$. However, u_r/r is due to a radial displacement, and so $\Delta\phi/\phi$ does not exactly equal $\epsilon_{\theta\theta}$, which leads us to call it a $\theta\theta$-type strain. We adopt the so-called Kirkwood model to account for $\Delta\phi/\phi$ in addition to the normal grain-grain interactions. Thus, we introduce angular springs of constant k^a acting between the edges V_1-V_2 and V_1-V_3 incident onto the node V_1, Fig. 18*d*; the edges remain straight throughout deformation.
- Central, shear and bending interactions: the total energy is
$$U=U^{\text{central}}+U^{\text{shear}}+U^{\text{moment}} \tag{6.3}$$
and, this model is a generalization of what we saw in Sections 4.1 and 4.2, depending on the type of beam chosen. This is a typical DE model, which, of course, may be

termed a locally inhomogeneous micropolar continuum, with inhomogeneity varying on the scale of grains; see Section 6.2 below.

- Central, shear, bending, and angular interactions: the total energy is

  One may argue that the three-point interaction should be introduced in the DE models so as to better represent the micromechanics, and to make, in accordance with Fig. 18*c*, the strain

  $$U=U^{\text{central}}+U^{\text{shear}}+U^{\text{moment}}+U^{\text{angular}} \tag{6.4}$$

  energy stored in a single Voronoi cell equal to Eq. (6.4). However, there exist successful DE models which account for normal and shear forces only [68,69]; this neglect of the contact moment is justified by the fact that only small numerical errors are thus caused in problems of interest in granular materials. In the case of a regular, triangular array of disks, this model is equivalent to a classical Born model of crystal lattices which is known to lack the rotational invariance [70].

6.2 Graph models of heterogeneous media

Let us pursue the planar graph representation of granular media in some more detail, Satake [71,72]. First, we list in Table 1 a correspondence between a system of rotund grains and its graph model. Besides the vertex and edge sets introduced earlier, we also have a loop set L.

Table 1.

assembly of grains	graph	index	number of elements
grain	vertex	v	$\|V\|$
contacting point	edge	e	$\|E\|$
void (in 2D)	loop	l	$\|L\|$

Table 2.

quantity	notation	number of elements	notation	quantity
body force	$\mathbf{B}^v$	$\|V\|$	$\mathbf{u}^v$	grain displacement
body couple	$\mathbf{N}^v$	$\|V\|$	$\mathbf{w}^e$	grain rotation
contact force	$\mathbf{F}^e$	$\|E\|$	$\Delta\mathbf{u}^e$	relative displacement
contact couple	$\mathbf{M}^e$	$\|E\|$	$\Delta\mathbf{w}^e$	relative rotation

With this geometric reference, we can set up an assignment of mechanical quantities—forces on the left and corresponding kinematic measures on the right—in Table 2.

The connectivity of the graph is described by the incidence matrix D^{ve}. Let us write down a total of $3|V|$ scalar equilibrium equations, each one with respect to a typical grain of radius r^v and volume V^v

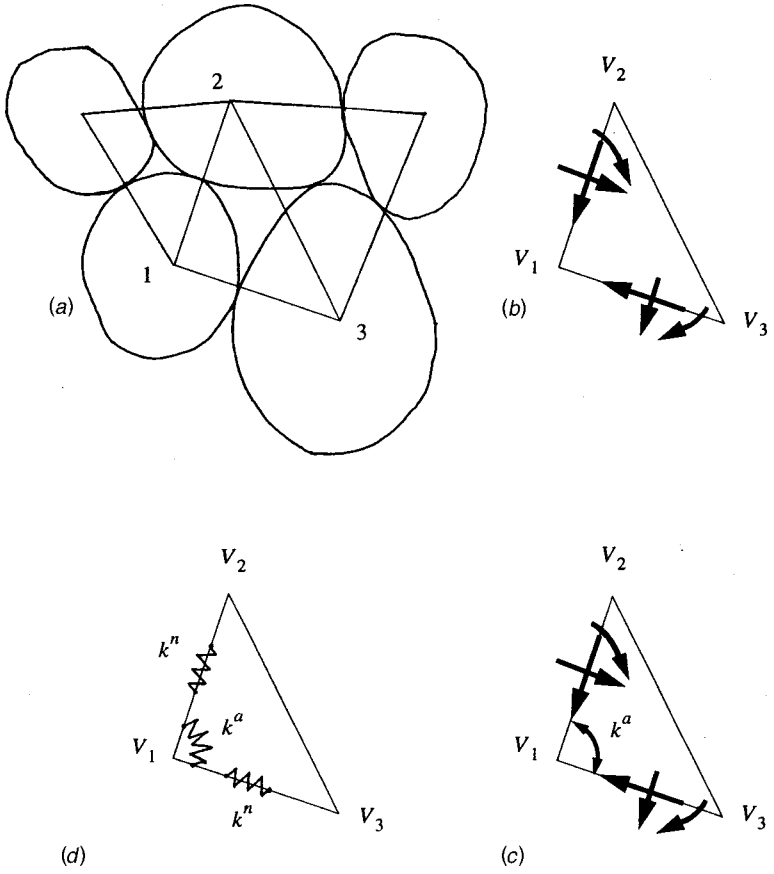

Fig. 18 *a*) A cluster of five grains showing the lines of interactions; *b*) a discrete element model showing the normal force, the shear force, and the moment exerted by grains 2 and 3 each onto the grain 1; *c*) a most general model showing the same grain-grain interactions as before but augmented by an internal, angular spring constant k^a; and *d*) a simplified model adopted in this paper, showing only normal (k^n) and angular (k^a) effects.

$$D^{\nu e}\begin{bmatrix}\boldsymbol{F}^e\\ \boldsymbol{M}^e\end{bmatrix}+\boldsymbol{V}^{\nu}\begin{bmatrix}\boldsymbol{B}^{\nu}\\ \boldsymbol{N}^{\nu}\end{bmatrix}=0 \tag{6.5}$$

where

$$\tilde{D}^{\nu e}=\begin{bmatrix}D^{\nu e} & 0\\ r^{\nu}D^{\nu e}\boldsymbol{n}^e\times & D^{\nu e}\end{bmatrix}. \tag{6.6}$$

Here $\boldsymbol{n}^e$ is the unit vector of edge e in the nonoriented graph. The operator (6.6) also plays a key role in the kinematics of all the edges

$$\begin{bmatrix}\Delta\boldsymbol{u}^e\\ \Delta\boldsymbol{w}^e\end{bmatrix}=-\tilde{D}^{e\nu}\begin{bmatrix}\boldsymbol{u}^{\nu}\\ \boldsymbol{w}^{\nu}\end{bmatrix} \tag{6.7}$$

where

$$\tilde{D}^{e\nu}=\begin{bmatrix}D^{e\nu} & -\boldsymbol{n}^e\times r^{\nu}D^{e\nu}\\ 0 & D^{e\nu}\end{bmatrix}. \tag{6.8}$$

The kinematics is subject to $3|L|$ compatibility constraints written for all the loops, where we make a reference to Satake's work.

The above should be augmented by $3|E|$ constitutive equations connecting the contact force $\boldsymbol{F}^e$ and contact moment $\boldsymbol{M}^e$ with the relative displacement $\Delta\boldsymbol{u}^e$ and relative rotation $\Delta\boldsymbol{w}^e$. Given 3 global equilibrium conditions, we have a total of

$$3(|V|-1+|E|+|L|)=6|E| \tag{6.9}$$

equations. Taking note of the Euler relation $|V|-|E|+|L|=1$, we see that this budget of equations agrees with the total of $6|E|$ unknowns-that is, $\boldsymbol{F}^e$, $\boldsymbol{M}^e$, $\Delta\boldsymbol{u}^e$ and $\Delta\boldsymbol{w}^e$-defined on edges of set E.

Finally, we note a formal analogy of (6.5) and (6.7) to the equilibrium and strain-displacement equations of Cosserat continua

$$Div\begin{bmatrix}\boldsymbol{\sigma}\\ \boldsymbol{\mu}\end{bmatrix}+\begin{bmatrix}\boldsymbol{b}\\ \boldsymbol{m}\end{bmatrix}=\boldsymbol{0}\quad \begin{bmatrix}\gamma\\ \kappa\end{bmatrix}=Grad\begin{bmatrix}\boldsymbol{u}\\ \boldsymbol{w}\end{bmatrix}. \tag{6.10}$$

A similarity of compatibility relations for the graph and the continuum descriptions has also been shown by Satake.

6.3 Periodic graphs with topological disorder

Randomness may be introduced into periodic networks in various ways. Figure 19 displays two basic possibilities: *substitutional* disorder and *topological* disorder. The first of these connotes a variability in properties per vertex (or node), while the second consists in a departure from the periodic topology and is therefore called a *topological disorder*. There is also a third case, of much more interest in solid state physics: *geometric disorder*, which involves the variability in the geometry of a network's structure—like uneven lengths of various bonds—but preserving a topological periodic structure [73]. The topological disorder is typically caused by an incompatibility of crystal-like domains in a granular material. The material may consist of equisized disks, which are organized into regular, periodic arrays, but the fact that they happen to be differently oriented in space causes an irregular structure and network of domain boundaries.

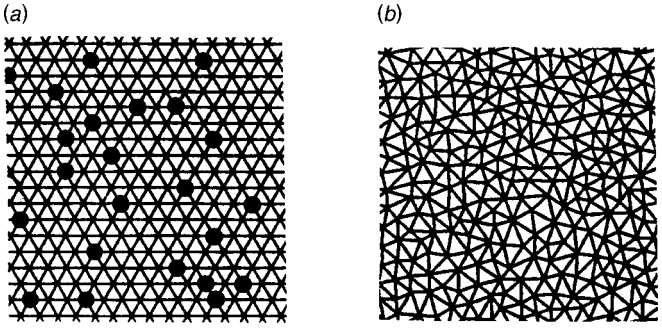

Fig. 19 Substitutional *a*) versus topological disorder *b*) of a hard-core Delaunay network

As observed earlier in connection with the DE model, the topological disorder leads to a locally inhomogeneous polar, or micropolar, continuum (depending on the type of vertex-vertex interactions) with inhomogeneity varying on the scale of grains. Such a continuum model contains a lot of information, but, in the first place, one wants to establish the *effective*, in the macroscopic sense, moduli $\boldsymbol{C}_L^{\text{eff}}$ of the material. For a non-polar (classical) continuum, these are obtained from the *periodic boundary conditions* on an $L\times L$ square B in 2D

$$u_i(\underset{\sim}{x}+\underset{\sim}{L})=u_i(\underset{\sim}{x})+\underset{\sim}{\varepsilon}_{ij}x_j\quad t_i(\underset{\sim}{x})=-t_i(\underset{\sim}{x}+\underset{\sim}{L})$$

$$\forall\underset{\sim}{x}\in\partial B. \tag{6.11}$$

Here $\overline{\boldsymbol{\epsilon}_{ij}}$ is the macroscopic strain, t_i is the traction on the boundary ∂B of B, and $\underset{\sim}{L}=L\underset{\sim}{e}_i$, with $\underset{\sim}{e}_i$ being a unit base vector. The periodicity means that the network topology is modified so as to repeat itself with some periodicity L in x_1 and x_2 directions, whereby L is usually taken much larger than the typical vertex-vertex spacing (or edge length).

Let us now consider a disordered, planar, granular medium, whose microstructural connectivity is modeled by a Poisson-Delaunay planar tessellation graph; it is generated from a realization of the Poisson point field in $\boldsymbol{R}^2$, eg, [58]. Now, the periodic conditions (6.11) require that a periodic network be set up, and this, in turn requires a periodic Poisson point field on the $L\times L$ square; topologically, this square is a torus.

A typical realization $\mathrm{B}(\omega)$ of a periodic Poisson-Delaunay network, numbering 200 vertices, is shown in Fig. 20. A set of all such realizations $\{\mathrm{B}(\omega);\omega\in\Omega\}$, where Ω is a sample space, forms a random medium B; a single ω indicates one realization of the Poisson point field and a chosen assignment of spring constants. In actual simulations, only a minute subset of the entire sample space can be investigated, but by the standard Monte Carlo and ergodicity arguments, this subset is representative of the whole system. Thus, already the response of a single network much larger than the grain size is sufficient to gain a good estimate of $\boldsymbol{C}_L^{\text{eff}}$ ($\equiv C_{ijkl}^{\text{eff}}$). The ensemble average of this tensor is isotropic for a microstructure of space-homogeneous and isotropic statistics, but even one realization of the network should be close to isotropic.

The procedure to calculate the effective moduli κ and $\mu$is as follows: a given B(ω) realization of the Delaunay network, is subjected, separately, to two tests: a biaxial extension $\overline{\epsilon}_{11}=\overline{\epsilon}_{22}$ and a shear deformation $\overline{\epsilon}_{11}=-\overline{\epsilon}_{22}$. Actual equilibrium state is found using a conjugate gradient method. Next, by equating, in each test, the network's energy to that of a 2D linear elastic equivalent continuum of area $V=L^2$

$$U=\frac{V}{2}\left[\kappa\overline{\varepsilon}_{ii}\overline{\varepsilon}_{jj}+2\mu\left(\overline{\varepsilon}_{ij}\overline{\varepsilon}_{ij}-\frac{1}{2}\overline{\varepsilon}_{ii}\overline{\varepsilon}_{jj}\right)\right] \tag{6.12}$$

the bulk and shear moduli, respectively, can be calculated directly. Repeating this process in a Monte Carlo sense for a number of realizations (so as to remove the fluctuations), the network's effective bulk and shear moduli are estimated.

In general, effective bulk and shear moduli display convex dependence on volume fraction that is characteristic of effective responses of many composite materials, eg [74]. Additionally, we observe a softening of these moduli relative to those corresponding to regular triangular networks-this is caused by the topological disorder. More details on these models, including a consideration of percolation in the case of very high contrast two-phase systems is given in [75,76].

Extensive studies of granular materials employing kinematic rather than periodic boundary conditions and truly large particle numbers, up to 50,000, were carried out by Rothenburg and co-workers, see [77–80]. Their solution method was based on the already mentioned quasi-static numerics of [67], with focus being, among others, on: homogenization and bounding via uniform strain or uniform stress assumptions; circular versus elliptical particles; and statistics of geometrical quantities and contact displacements under compressive and shearing loading.

APPENDIX: PLANAR CONTINUUM ELASTICITY

The constitutive relations of a linear elastic, isotropic 3D continuum are

$$\varepsilon_{11}=\frac{1}{E_{3D}}[\sigma_{11}-\nu_{3D}(\sigma_{22}+\sigma_{33})] \quad \varepsilon_{12}=\frac{1+\nu_{3D}}{E_{3D}}\sigma_{12} \tag{A.1}$$

together with cyclic permutations $1\rightarrow2\rightarrow3$, or, equivalently,

$$\sigma_{ij}=\lambda_{3D}\varepsilon_{kk}\delta_{ij}+2\mu_{3D}\varepsilon_{ij} \quad i,j,k=1,...,3. \tag{A.2}$$

Here E_{3D}, ν_{3D}, λ_{3D} and μ_{3D} stand for the conventional 3D Young's modulus, Poisson's ratio, and Lamé constants, all the relations between these moduli being well known.

On the other hand, in 2D (or *planar*) elasticity, there is no x_3 direction and so ε_{11}, ε_{22}, ε_{12} are the only strains and σ_{11}, σ_{22}, σ_{12} the only stresses. Thus, we have

$$\varepsilon_{11}=\frac{1}{E}[\sigma_{11}-\nu\sigma_{22}] \quad \varepsilon_{12}=\frac{1+\nu}{E}\sigma_{12} \tag{A.3}$$

with cyclic permutation $1\rightarrow2$, or, equivalently,

$$\varepsilon_{ij}=\frac{1+\nu}{E}\left[\sigma_{ij}-\frac{\nu}{1+\nu}\sigma_{kk}\delta_{ij}\right] \quad i,j,k=1,...,2. \tag{A.4}$$

In these equations, we introduce a rule of writing the 2D moduli without any subscripts, so that E and ν stand for the *2D (or planar) Young's modulus* and *2D Poisson's ratio* [16]; some authors [81] use the term area moduli. Now, in analogy to (*A*.2) above, we introduce the 2D λ and μ moduli by writing

$$\sigma_{ij}=\lambda\varepsilon_{kk}\delta_{ij}+2\mu\varepsilon_{ij} \tag{A.5}$$

and find the relations

$$E=4\mu\frac{\lambda+\mu}{\lambda+2\mu} \quad \nu=\frac{\lambda}{\lambda+2\mu}. \tag{A.6}$$

Just like in the 3D elasticity, from three tests—uniaxial stress, hydrostatic stress, and simple shearing stress—one can work out basic inequalities that hold between these planar moduli

$$\lambda+2\mu>0 \quad \lambda+\mu>0 \quad \mu>0 \tag{A.7}$$

whereby we note that the planar shear modulus is given by the same formula in 2D as in 3D. If μ obeys the third of these inequalities, the first one is a consequence of the second and can be dropped. It is easy to see that, Poisson's ratio given by $(A.6)_2$ assumes the value -1, and, since

$$\frac{\partial\nu}{\partial\lambda}=2\frac{\mu}{(\lambda+2\mu)^2}>0 \tag{A.8}$$

ν increases monotonically on any vector $\boldsymbol{q}$ parallel to the λ axis in the λ, μ-plane, tending towards 1 with -1 increasing distance from Q. Thus we note that ν ranges from -1 through $+1$, in contradistinction to ν_{3D}, which is bounded by -1 and 1/2. Now, an inspection of $(A.1)_2$ immediately

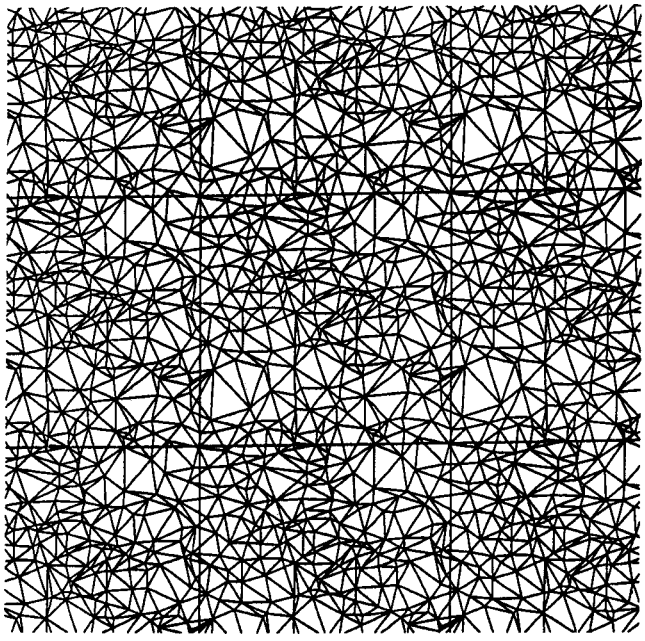

Fig. 20 A periodic Poisson-Delaunay network with 200 vertices

reveals that the planar shear modulus does not change, while applying the concept of bulk modulus to relations $(A.1)_1$, we infer the planar bulk modulus κ, that is

$$\kappa=\frac{E}{2(1-\nu)} \quad \mu=\frac{E}{2(1+\nu)}. \tag{A.9}$$

Two other very useful relations linking these two-dimensional moduli E, ν, κ, and μ can readily be inferred

$$\frac{4}{E}=\frac{1}{\kappa}+\frac{1}{\mu} \quad \nu=\frac{\kappa-\mu}{\kappa+\mu}. \tag{A.10}$$

Upon substitution of (A.5) into the balance law $\sigma_{ij,j}=0$, we find a planar Navier's equation for the displacement u_i (see also, [45,46])

$$\mu u_{i,jj}+\kappa u_{j,ji}=0. \tag{A.11}$$

We now examine the relation of planar elasticity to two well known special cases of 3D elasticity.

Plane strain

In that case, one requires $u_3=0$ in Eqs. (A.1)–(A.2) along with the independence of all the fields with respect to the x_3 direction, so that $\varepsilon_{33}=\varepsilon_{31}=\varepsilon_{32}=0$ and

$$\varepsilon_{11}=\frac{1}{E_{3D}}[(1-\nu_{3D}{}^2\sigma_{11}-(\nu_{3D}-\nu_{3D}{}^2)\sigma_{22}$$

$$\varepsilon_{12}=\frac{1+\nu_{3D}}{E_{3D}}\sigma_{12} \tag{A.12}$$

again with the cyclic permutation $1\rightarrow 2$. A comparison with Eq. (A.3) readily shows that the following relationships between the 2D and the 3D moduli hold

$$\frac{1}{E}=\frac{1+\nu_{3D}{}^2}{E_{3D}} \quad \frac{\nu}{E}=\frac{\nu_{3D}+\nu_{3D}{}^2}{E_{3D}} \quad \frac{1+\nu}{E}=\frac{1+\nu_{3D}}{E_{3D}}. \tag{A.13}$$

This is a mapping of two constants onto two constants, so that only two relations of the above three are independent, and it is easy to check that Eq. $(A.13)_3$ is redundant. Of particular interest is the relation between the plane strain Poisson's ratio and the 3D Poisson's ratio

$$\nu=\frac{\nu_{3D}}{1-\nu_{3D}}. \tag{A.14}$$

Clearly, the case of $\nu=+1$ represents a planar incompressible material corresponding to the 3D incompressible material of $\nu_{3D}=1/2$.

Plane stress

In that case, one requires $\sigma_{33}=\sigma_{31}=\sigma_{32}=0$ and the independence of all the fields with respect to the x_3 direction, which leads to

$$\varepsilon_{11}=\frac{1}{E}[\sigma_{11}-\nu\sigma_{22}] \quad \varepsilon_{12}=\frac{1+\nu}{E}\sigma_{12} \tag{A.15}$$

with cyclic permutation $1\rightarrow 2$. A comparison with Eq. (A.3) readily shows that the following relationships between the two-dimensional (plane-stress) and the three-dimensional moduli hold

$$\frac{1}{E}=\frac{1}{E_{3D}} \quad \frac{\nu}{E}=\frac{\nu_{3D}}{E_{3D}} \quad \frac{1+\nu}{E}=\frac{1+\nu_{3D}}{E_{3D}} \tag{A.16}$$

The third of these relations is redundant, but the most important thing is that

$$E=E_{3D} \quad \nu=\nu_{3D} \quad \mu=\mu_{3D}=\frac{E}{2(1+\nu)} \tag{A.17}$$

while the 2D bulk modulus κ is

$$\kappa=\frac{E}{2(1-\nu)} \tag{A.18}$$

Note that Eqs. (A.9)–(A.10) hold again.

Relations of planar isotropic elasticity shown here may be generalized to orthotropic and general anisotropic materials.

REFERENCES

[1] Hrennikoff A (1941), Solution of problems of elasticity by the framework method, *ASME J. Appl. Mech.* **8**, A619–A715.
[2] Maxwell JC (1869), *Scientific Papers II*.
[3] Askar A (1985), *Lattice Dynamical Foundations of Continuum Theories*, World Scientific, Singapore.
[4] Noor AK and Nemeth MP (1980), Micropolar beam models for lattice grids with rigid joints, *Comput. Methods Appl. Mech. Eng.* **21**, 249–263.
[5] Triantafyllidis N and Bardenhagen S (1993), On higher order gradient continuum theories in 1-D nonlinear elasticity. Derivation from and comparison to the corresponding discrete models, *J. Elast.* **33**, 259–293.
[6] Stephen NG and Wang PJ (1996), On Saint-Venant's principle in pinjointed frameworks, *Int. J. Solids Struct.* **33**(1) 79–97.
[7] Noor AK (1988), Continuum modeling for repetitive lattice structures, *Appl. Mech. Rev.* **41**(7) 285–296.
[8] Costello GA (1997), *Theory of Wire Rope*, Springer-Verlag.
[9] Lakes RS and Benedict R (1982), Noncentrosymmetry in micropolar elasticity, *Int. J. Eng. Sci.* **29**(10) 1161–1167.
[10] Nowacki W (1986), *Theory of Asymmetric Elasticity*, Oxford: Pergamon Press/Warsaw: PWN-Polish Scientific Publ.
[11] Blouin F and Cardou A (1974), A study of helically reinforced cylinders under axially symmetric loads and application to strand mathematical modeling, *Int. J. Solids Struct.* **25**(2) 189–200.
[12] Samras RK, Skop RA, and Milburn DA (1974), An analysis of coupled extensional-torsional oscillations in wire rope, *ASME J. Eng. Ind.* **96**, 1130–1135.
[13] Love AEH (1934), *The Mathematical Theory of Elasticity*, Cambridge Univ Press.
[14] Grah M, Alzebdeh K, Sheng PY, Vaudin MD, Bowman KJ, and Ostoja-Starzewski M (1996), Brittle intergranular failure in 2D microstructures: experiments and computer simulations, *Acta Mater.* **44**(10) 4003–4018.
[15] Kirkwood JG (1939), The skeletal modes of vibration of long chain molecules, *J. Chem. Phys.* **7**, 506–509.
[16] Thorpe MF and Jasiuk I (1992), New results in the theory of elasticity for two-dimensional composites *Proc. R. Soc. London, Ser. A* **A438**, 531–544.
[17] Day AR, Snyder KA, Garboczi EJ, and Thorpe MF (1992), The elastic moduli of a sheet containing circular holes, *J. Mech. Phys. Solids* **40**, 1031–1051.
[18] Keating PN (1966), Effect of invariance requirements on the elastic strain energy of crystals with application to the diamond structure, *Phys. Rev.* **145**, 637–645.
[19] Synder KA, Garboczi EJ, and Day AR (1992), The elastic moduli of simple two-dimensional composites: computer simulation and effective medium theory, *J. Mech. Phys. Solids* **72**, 5948–5955.

[20] Press WH, Teukolsky SA, Vetterling WT, and Flannery BP (1992), *Numerical Recipes*, Cambridge Univ Press.

[21] Chung JW, Roos A, De Hosson JTh M, and van der Giessen E (1996), Fracture of disordered three-dimensional spring networks: A computer simulation methodology, *Phys. Rev. B* **54**, 15094–15100.

[22] Ostoja-Starzewski M and Schulte J (1996), Bounding of effective thermal conductivities of multiscale materials by essential and natural boundary conditions, *Phys. Rev. B* **54**, 278–285.

[23] Ostoja-Starzewski M (1998), Random field models of heterogeneous materials, *Int. J. Solids Struct.* **35**(19) 2429–2455.

[24] Garboczi E (1998), *Finite Element Programs and Finite Difference Programs for Computing the Linear Electric and Elastic Properties of Digital Images of Random Materials*, NISTIR 6269, NIST, Gaithersburg MD.

[25] Torquato S (1997), Effective stiffness tensor of composite media, *J. Mech. Phys. Solids* **45**, 1421–1448.

[26] Keller JB (1964), A theorem on the conductivity of a composite medium, *J. Math. Phys.* **5**, 548–549.

[27] Mendelson KS (1975), Effective conductivity of two-phase material with cylindrical phase boundaries, *J. Appl. Phys.* **46**, 917–918.

[28] Cherkaev AV, Lurie KA, and Milton GW (1992), Invariant properties of the stress in plane elasticity and equivalence classes of composites, *Proc. R. Soc. London, Ser. A* **A438**, 519–529.

[29] Ostoja-Starzewski M and Jasiuk I (1995), Stress invariance in planar Cosserat elasticity, *Proc. R. Soc. London, Ser. A* **451**, 453–470. errata: **452**, 1503 (1995).

[30] Wozniak C (1970), *Surface Lattice Structures* (in Polish), Polish Sci Publ, Warsaw.

[31] Gulati in [32].

[32] Gibson LJ and Ashby MF (1988), *Cellular Solids*, Pergamon Press.

[33] Ostoja-Starzewski M, Sheng PY, and Alzebdeh K (1996), Spring network models in elasticity and fracture of composites and polycrystals, *Comput. Mater. Sci.* **7**(1,2) 82–93.

[34] Jasiuk I, Chen J, and Thorpe MF (1994), Elastic moduli of two dimensional materials with polygonal holes, *Appl. Mech. Rev.* **47** (1, Pt 2) S18–S28.

[35] Jasiuk I (1995), Polygonal cavities vis-à-vis rigid inclusions: Effective elastic moduli of materials with polygonal inclusions, *Int. J. Solids Struct.* **32**, 407–422.

[36] Stalne K and Gustafson PJ (2001), A three dimensional finite element fibre model for composite material stiffness and hygroexpansion analysis, *Proc. 2nd Eur. Conf. Comp. Mech. ECCM-2001*, Cracow, Poland.

[37] Wozniak C (1997), Internal variables in dynamics of composite solids with periodic microstructure, *Arch. Mech.* **49**(2) 421–441.

[38] Wozniak C (1966), Load carrying structures of dense lattice type, *Arch. Mech. Stos.* **18**(5) 581–597.

[39] Cielecka I, Wozniak C, and Wozniak M (1998), Internal variables in macrodynamics of two-dimensional periodic cellular media, *Arch. Mech.* **50**(1) 3–19.

[40] Pshenichnov GI (1993), *A Theory of Latticed Plates and Shells*, World Scientific, Singapore.

[41] Cioranescu D and Saint Jean Paulin J (1999), *Homogenization of Reticulated Structures*, Springer Verlag, New York.

[42] Holnicki-Szulc J and Rogula D (1979a), Non-local, continuum models of large engineering structures, *Arch. Mech.* **31**(6) 793–802.

[43] Holnicki-Szulc J and Rogula D (1979b), Boundary problems in nonlocal, continuum models of large engineering structures, *Arch. Mech.* **31**(6) 803–811.

[44] Bardenhagen S, and Triantafyllidis N (1994), Derivation of higher order gradient continuum theories in 2,3-D non-linear elasticity from periodic lattice models, *J. Mech. Phys. Solids* **42**, 111–139.

[45] Wan XL and Stronge WJ (1999), Micropolar theory for two-dimensional stresses in elastic honeycomb, *Proc. R. Soc. London, Ser. A* **455**, 2091–2116.

[46] Chen JY, Huang Y, and Ortiz M (1998), Fracture analysis of cellular materials: A strain gradient model, *J. Mech. Phys. Solids* **46**, 789–828.

[47] Crapo H and Whiteley W (1989), The geometry of rigid structures, in *Encyclopedia of Mathematics and its Applications*, Cambridge Univ Press.

[48] Laman (1970), On graphs and rigidity of plane skeletal structures, *Eng. Math.* **4**, 331–340.

[49] Asimov L and Roth B (1978), The rigidity of graphs, *Trans. Am. Math. Soc.* **245**, 279–289.

[50] Feng S, Thorpe MF, and Garboczi E (1985), Effective-medium theory of percolation on central-force elastic networks, *Phys. Rev. B* **31**, 276–280.

[51] Boal DH (1993), Rigidity and connectivity percolation in heterogeneous polymer-fluid networks, *Phys. Rev. E* **47**, 4604–4606.

[52] Hansen JC, Chien S, Skalak R, and Hoger A (1996), An elastic network model based on the structure of the red blood cell membrane skeleton, *Biophys. J.* **70**, 146–166.

[53] Miles RE (1964), Random polygons determined by random lines in a plane, *Proc. Natl. Acad. Sci. U.S.A.* **52**, 901–907.

[54] Cox HL (1952), The elasticity and strength of paper and other fibrous materials, *Br. J. Appl. Phys.* **3**, 72–79.

[55] Page DH, Tydeman PA, and Hunt M (1961), A study of fibre-to-fibre bonding by direct observation, *The Formation and Structure of Paper—Trans. Oxford Symp* **1**, 171–193.

[56] Ostoja-Starzewski M, Quadrelli MB, and Stahl DC (1999), Kinematics and stress transfer in quasi-planar random fiber networks, *C. R. Acad. Sci., Ser. IIb: Mec., Phys., Chim., Astron.* **327**, 1223–1229.

[57] Stahl DC and Cramer SM (1988), A three-dimensional network model for a low density fibrous composite, *ASME J. Eng. Mater. Technol.* **120**(2) 126–130.

[58] Chung JW, Roos A, De Hosson JThM, and van der Geissen E (1996), Fracture of disordered three-dimensional spring networks: A computer simulation methodology, *Phys. Rev. B* **54**(21) 15094–15100.

[59] Sastry AM, Cheng X, and Wang CW (1998), Mechanics of stochastic fibrous networks, *J. Thermoplast. Compos. Mater.* **11**, 211–296.

[60] Cheng X, and Sastry AM (1999), On transport in stochastic, heterogeneous fibrous domains, *Mech. Mater.* **31**, 765–786.

[61] Cook RD, Malkus ME and Plesha ME (1989), *Concepts and Applications of Finite Element Analysis*, John Wiley & Sons, New York.

[62] Stoyan D, Kendall WS, and Mecke J (1987), *Stochastic Geometry and its Applications*, John Wiley & Sons, New York.

[63] Kuznetsov EN (1991), *Underconstrained Structural Systems*, Springer-Verlag, New York.

[64] Kellomaki M, Aström J, and Timonen J (1996), Rigidity and dynamics of random spring networks, *Phys. Rev. Lett.* **77**(13) 2730–2733.

[65] Raisanen VI, Alava MJ, and Nieminen RM (1997), Failure of planar fiber networks, *J. Appl. Phys.* **82**(8) 3747–3753.

[66] Ostoja-Starzewski M, and Stahl DC (2000), Random fiber networks and special elastic orthotropy of paper, *J. Elast.* **60**(2), 131–149.

[67] Cundall PA, and Strack ODL (1979), A discrete numerical model for granular assemblies, *Geotechnique* **29**(1) 47–65.

[68] Bathurst RJ, and Rothenburg L (1988), Micromechanical aspects of isotropic granular assemblies with linear contact interactions, *ASME J. Appl. Mech.* **55**, 17–23.

[69] Bathurst RJ, and Rothenburg L (1989), Note on a random isotropic granular material with negative Poisson's ratio, *Int. J. Eng. Sci.* **26**, 373–383.

[70] Jagota A and Benison SJ (1994), Spring-network and finite-element models for elasticity and fracture, in *Non-linearity and Breakdown in Soft Condensed Matter*, KK Bardhan, BK Chakrabarti, and A Hansen (eds), *Lecture Notes in Physics* **437**, Springer-Verlag, NY, 186–201.

[71] Satake M (1976), Constitution of mechanics of granular materials through graph representation, *Proc. 26th Japan Natl. Congr. Theor. Appl. Mech.*, 257–266.

[72] Satake M (1978), Constitution of mechanics of granular materials through the graph theory, *Continuum Mechanical and Statistical Approaches in the Mechanics of Granular Materials*, SC Cowin and M Satake (eds), 47–62.

[73] Ziman JM (1979), *Models of Disorder*, Cambridge University Press.

[74] Torquato S (1991), Random heterogeneous media: microstructure and improved bounds on effective properties, *Appl. Mech. Rev.* **44**(2) 37–76.

[75] Ostoja-Starzewski M, Alzebdeh K, and Jasiuk I (1995), Linear elasticity of planar Delaunay networks-III: Self-consistent approximations, *Acta Mech.* **110**, 57–72.

[76] Alzebdeh K and Ostoja-Starzewski M (1999), On a spring network model and effective elastic moduli of granular materials, *ASME J. Appl. Mech.* **66**, 172–180.

[77] Kruyt NP and Rothenburg L (1996), Micromechanical definition of the strain tensor for granular materials, *ASME J. Appl. Mech.* **63**, 706–711.

[78] Kruyt NP and Bathurst RJ (1998), Statistical theories for the elastic moduli of two-dimensional assemblies of granular materials, *Int. J. Eng. Sci.* **36**, 1127–1142.

[79] Kruyt NP and Rothenburg L (2001), Statistics of the elastic behaviour of granular materials, *Int. J. Solids Struct.* **38**, 4879–4899.

[80] Rothenburg L and Bathurst RJ (1996), Micromechanical features of granular assemblies with planar particles, *Geotechnique* **42**, 79–95.

[81] Cherkaev A (2000), *Variational Methods for Structural Optimization*, Springer-Verlag.

Following undergraduate education at the Cracow University of Technology (Poland) ***Martin Ostoja-Starzewski*** *obtained Masters and PhD degrees at McGill University, all in mechanical engineering. In 2001, subsequent to academic posts at Purdue University, Michigan State University, and the Institute of Paper Science and Technology (with adjunct faculty position at Georgia Tech), he was appointed to the Canada Research Chair in Mechanics of Materials at McGill University. He was a Visiting Scientist at Cornell University, at the Institute for Mechanics and Materials at UCSD, at EPFL (Switzerland), Ecole des Mines de Paris (France), and at Ecole Polytechnique (France). He has published over 65 journal papers in applied/theoretical mechanics, materials science, applied mathematics/physics and geophysics, and over 70 conference proceedings papers. His research is in stochastic and computational mechanics with focus on mechanics and transport phenomena in random media, including: micropolar continuum mechanics; scale effects in elasticity, plasticity, and fracture/damage in composites; random fields and stochastic finite elements; stochastic waves. From 1998 to 2001, he chaired the ASME Committee on Constitutive Equations and was recently elected an ASME Fellow. He (co-)edited 7 books and (co-)organized many symposia and conferences, including a NATO Advanced Research Workshop, as well as a course on Mechanics of Random and Multiscale Microstructures at CISM.*